

Chemistry–A European Journal

Supporting Information

Unravelling the Role of Structural Factors in the Luminescence Properties of Persulfurated Benzenes

Andrea Fermi,* Simone D'Agostino,* Yasi Dai, Filippo Brunetti, Fabrizia Negri,* Marc Gingras,
and Paola Ceroni

– SUPPORTING INFORMATION –

SYNTHETIC PROCEDURES	2
XRD ANALYSIS.....	4
DSC ANALYSIS	8
PHOTOPHYSICAL CHARACTERIZATION.....	13
COMPUTATIONAL DETAILS	20
SUPPORTING REFERENCES	37

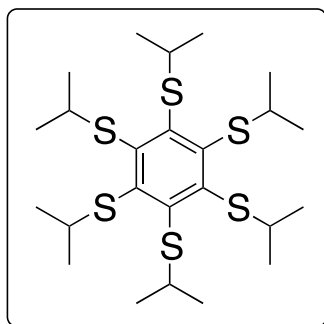
SYNTHETIC PROCEDURES

General information: ^1H -NMR and ^{13}C -NMR spectra were recorded on Varian Mercury 400 MHz spectrometer or on a Bruker Avance 600 spectrometer. The chemical shifts (δ) for ^1H are given in ppm relative to residual signals of the solvents (CDCl_3 : $\delta = 7.26$ ppm). Data are reported as follows: chemical shift (δ), multiplicity (s = singlet, d = doublet, t = triplet, q = quartet, dd = doublet of doublets, m = multiplet, etc.), coupling constants (Hz). The chemical shifts (δ) for ^{13}C are given in ppm relative to residual signals of the solvents and tetramethylsilane (TMS) at 0 ppm (CDCl_3 : $\delta = 77.16$ ppm). GC-MS spectra were taken by EI ionization at 70 eV on a Hewlett-Packard 5971 with GC injection. Chromatographic purifications were done with 240-400 mesh silica gel. All reactions were set up under an argon or nitrogen atmosphere in oven-dried glassware using standard Schlenk techniques. Unless specified, other anhydrous solvents were used without further purifications. All reagents were purchased from commercial suppliers (Sigma-Aldrich, Alfa Aesar, Fluorochem, TCI, etc.) and used without further purification unless specified.

Synthesis of A6-Ph, A6-pTol, A6-oTol, A6-iPr

The synthetic procedure for these compounds has been reported elsewhere.^[1-3]

Synthesis of B6-iPr



This synthesis is a slightly modified procedure compared to the protocol reported in *J. Org. Chem.* **1980**, *45*, 4376–4380.

In a flame dried 250 mL two-necked round bottom flask equipped with a magnetic stirring bar, under nitrogen atmosphere, C_6F_6 (115 μl , 1.0 mmol, 1 equiv.), NaH (263 mg, 11.0 mmol, 11 equiv.) and dry DMF (10 ml) are added and the mixture allowed to stir for 10 minutes at RT. The mixture is then cooled at ca. 0°C (ice bath) and $i\text{PrSH}$ (925 μl , 10.0 mmol, 10 equiv.) is carefully added dropwise (ca. 10 minutes, vigorous bubbling), while the solution gets a yellow color. The mixture is let to stir overnight at RT. After

18 hrs, water is carefully added (20 ml) and the precipitate extracted with diethyl ether (3x10 ml). Once the organic layers have been combined and dried over MgSO_4 , solvents are evaporated; the crude solid product is then purified by flash chromatography (SiO_2 , hexane:diethyl ether 98:2) and finally crystallized twice from slow evaporation of CHCl_3 : CH_3OH (1:1, v/v) to afford 49 mg (0.094 mmol) of hexakis(isopropylthio)benzene as a yellow crystalline solid (**B6-iPr**, yield 9%) in high purity. ^1H and ^{13}C NMR characterization is consistent with literature reports.^[4]

^1H NMR (400 MHz, CDCl_3 , ppm): $\delta = 1.16$ (d, $J = 1.2$ Hz, 36 H), 3.76 (septet, $J = 3.8$ Hz, 6 H); ^{13}C NMR (101 MHz, CDCl_3 , ppm): 22.87 (12 C), 41.02 (6 C), 146.09 (6 C). LRMS (m/z, %): 522 (100%, M), 480 (3%, M- C_3H_6), 437 (4%, M- $2\text{C}_3\text{H}_6$), 395 (13%, M- $3\text{C}_3\text{H}_6$), 353 (25%, M- $4\text{C}_3\text{H}_6$), 311 (42%, M- $5\text{C}_3\text{H}_6$), 269 (15%, M- $6\text{C}_3\text{H}_6$).

NMR data

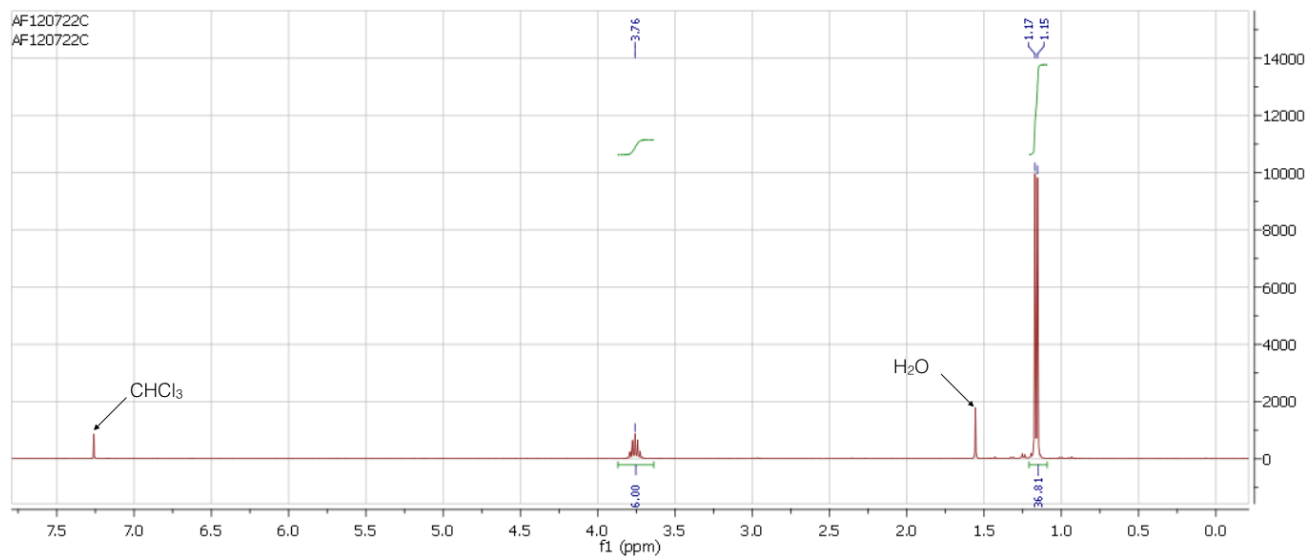


Figure S1. ¹H NMR of B6-iPr (400 MHz, CDCl₃).

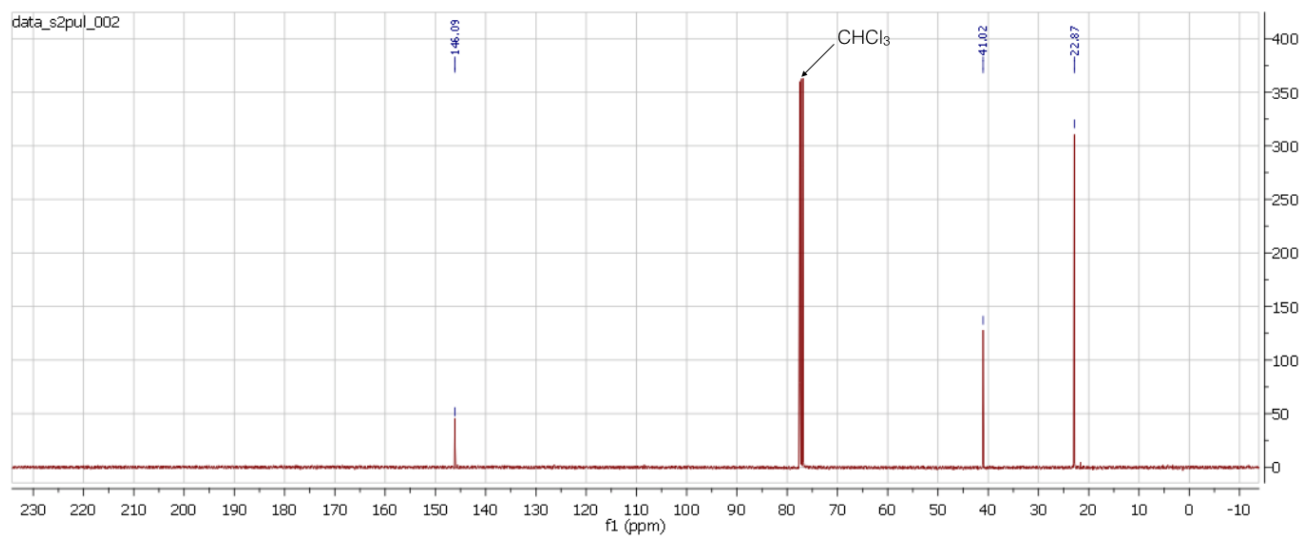


Figure S2. ¹³C NMR of B6-iPr (101 MHz, CDCl₃).

XRD ANALYSIS

Data for **B6-iPr** were collected at both at RT and low temperature (110 K) on a Bruker D8 Venture diffractometer equipped with a PHOTON III detector, a μ S 3.0 microfocus X-ray source (Cu $K\alpha$ radiation, $\lambda = 1.54056 \text{ \AA}$), and a cryostat Oxford CryoStream800. Data for **A6-iPr** were collected at RT on an Oxford X'Calibur S CCD diffractometer equipped with a graphite monochromator (Mo- $K\alpha$ radiation, $\lambda = 0.71073 \text{ \AA}$). All the structures were solved with SHELXT^[5] by intrinsic phasing and refined on F^2 with SHELXL^[6] implemented in the Olex² software^[7] by full-matrix least squares refinement. H_{CH} atoms for all compounds were added in calculated positions and refined riding on their respective carbon atoms. All non-hydrogen atoms were anisotropically refined and the rigid-body RIGU restraints applied.^[5] See Table S1 for crystallographic details. Crystal data can be obtained free of charge via <https://www.ccdc.cam.ac.uk/structures/> (or e-mail: deposit@ccdc.cam.ac.uk); CCDC numbers 2330031-2330033. For phase identification purposes, X-ray powder diffractograms in the 2θ range $5\text{-}40^\circ$ (step size, 0.02° ; time/step, 20 s; 0.04 rad soller; $40\text{mA} \times 40\text{kV}$) were collected on a Panalytical X'Pert PRO automated diffractometer equipped with an X'Celerator detector and in Bragg-Brentano geometry, using Cu $K\alpha$ radiation without a monochromator, and for variable temperature XRD measurements, with an Anton-Paar TTK 450 + LNC. The software Mercury^[8] was used to calculate the X-ray powder patterns based on single crystal data collected in this work or retrieved from CCDC. For all compound, the identity between polycrystalline samples and single crystals was verified by comparing experimental and calculated powder diffraction patterns (See Figure S3). VT-XRD patterns for **B6-iPr** and **A6-iPr** were not collected due to the small amount of materials available.

Table S1. Crystal data and refinement details for crystalline **B6-iPr** (both at RT and 110 K) and **A6-iPr** at RT.

	B6-iPr (RT)	B6-iPr (110 K)	A6-iPr
Formula	$C_{12}H_{21}S_3$	$C_{12}H_{21}S_3$	$C_{60}H_{66}S_6$
fw	261.47	261.47	979.48
Temperature (K)	300	110	300
Cryst. System	Triclinic	Triclinic	Monoclinic
Space group	P-1	P-1	P2/c
Z	2	2	4
a (Å)	9.3418(4)	9.1088(6)	19.9777(7)
b (Å)	9.7038(5)	9.5723(6)	11.6190(3)
c (Å)	10.1564(5)	9.8544(6)	25.1875(8)
α (deg)	71.797(2)	72.176(2)	90
β (deg)	71.170(2)	71.961(2)	106.263(3)
γ (deg)	64.968(2)	63.870(2)	90
V (Å³)	772.79(7)	718.85(8)	5612.6(3)
D_{calc} (g/cm³)	1.124	1.208	1.159
μ (mm⁻¹)	4.141	4.452	0.280
Meas.d refln.s	20497	21040	31504
Indep refln.s	2845	2617	13138
Largest diff. peak/hole (e/Å³)	0.25/-0.19	0.57/-0.40	0.304 / -0.310
R₁[on F₀², I>2σ(I)]	0.0531	0.0341	0.0683
wR₂ (all data)	0.1766	0.0882	0.1510

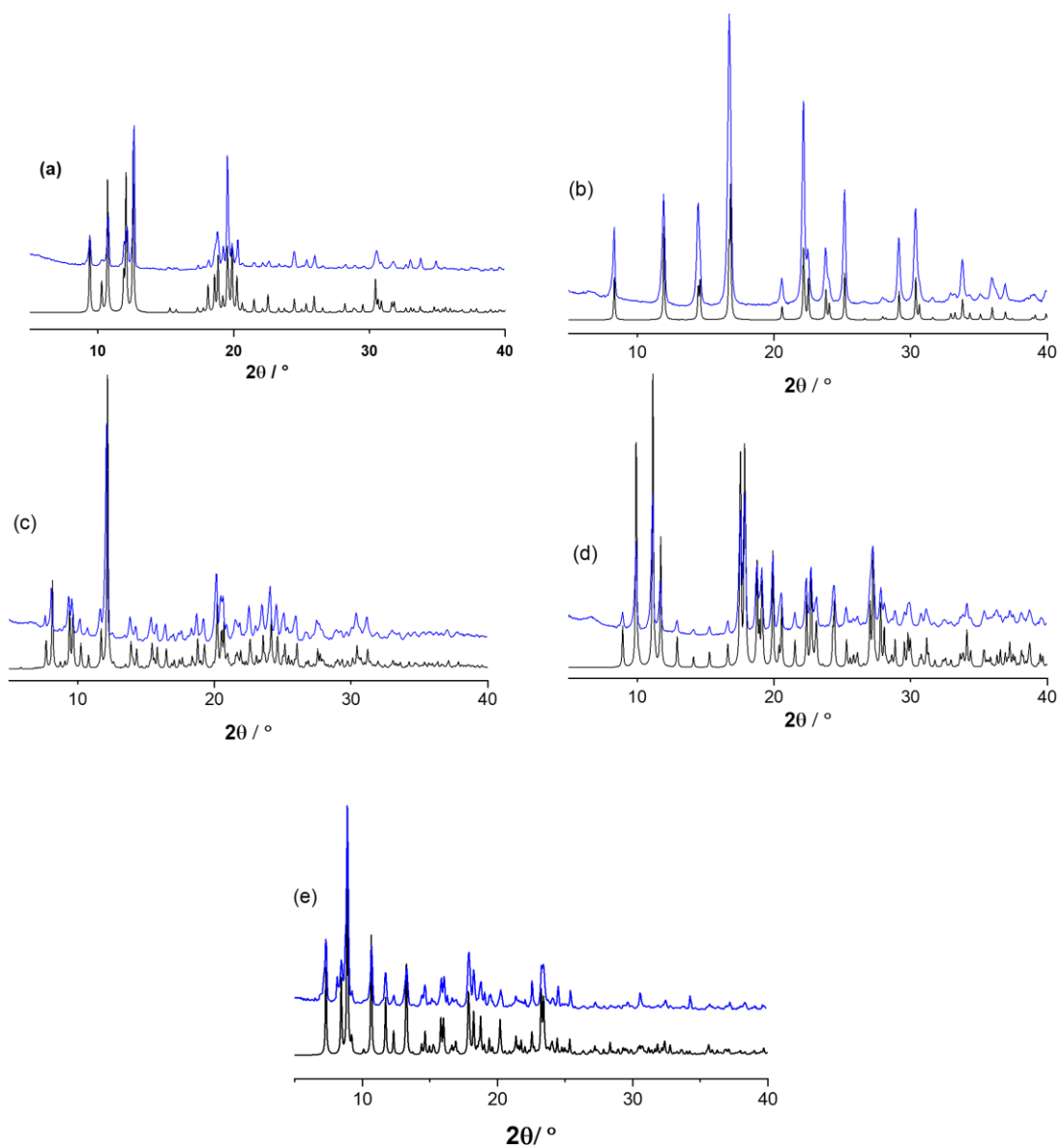


Figure S3. Comparison between calculated (black lines) and experimental (blue lines) powder XRD patterns collected at RT for (a) **B6-iPr**, (b) **A6-pTol** (CSD refcode: VEMGIG), (c) **A6-oTol** (CSD refcode: GEGLAF), (d) **A6-Ph** (CSD refcode: ZERJEL02), and (e) **A6-iPr**.

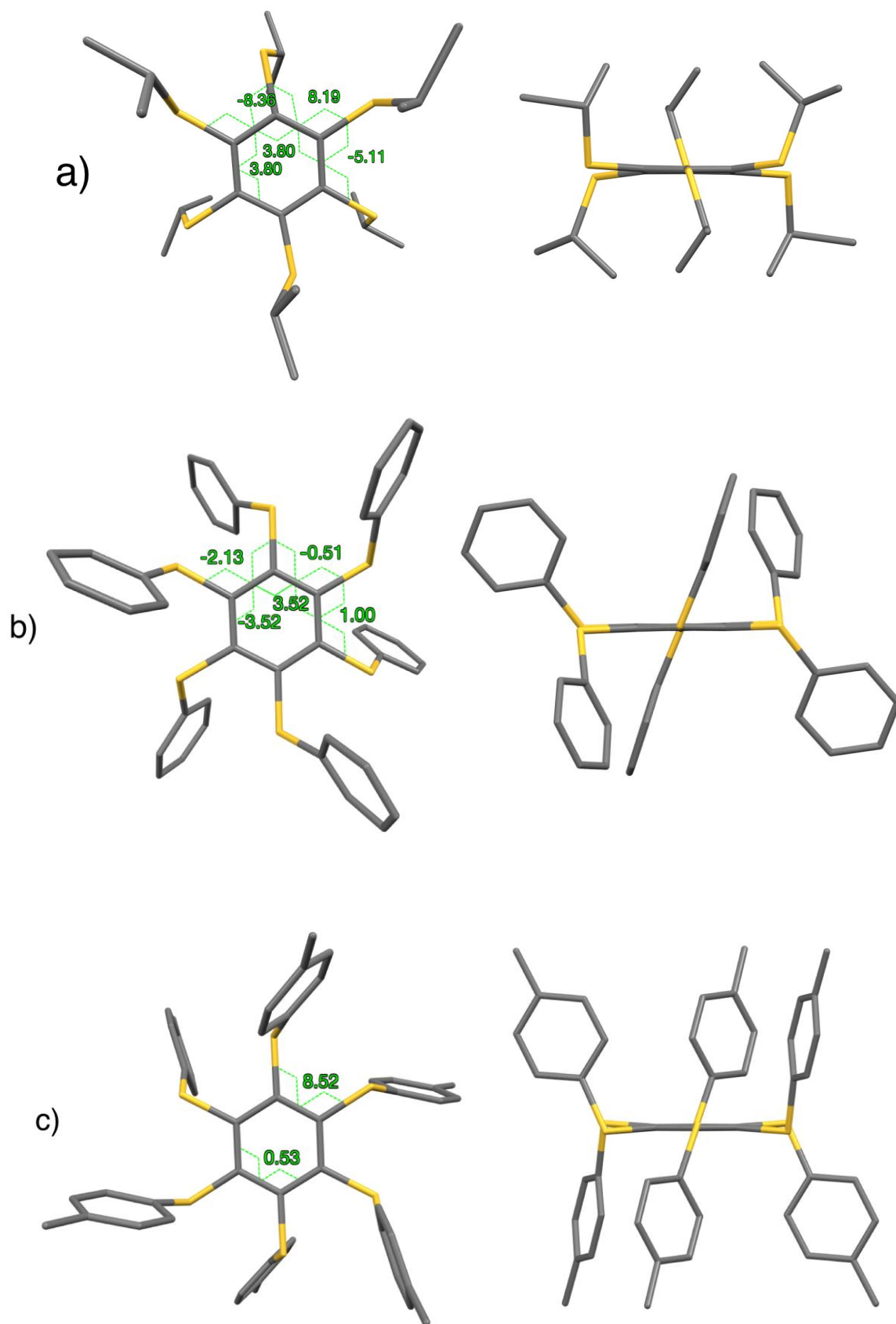


Figure S4. Torsion angles in degrees between core (CC-CC) and peripheral (SC-CS) bonds in crystals of **B6-iPr** (a), **A6-Ph** (b) and **A6-pTol** (c). Data for **A6-Ph** and **A6-pTol** are taken from published results^[3] (CCDC refcodes: ZERJEL02 and VEMGIG, respectively). Side views are also shown for each compound (right side). Hydrogen atoms are omitted for clarity.

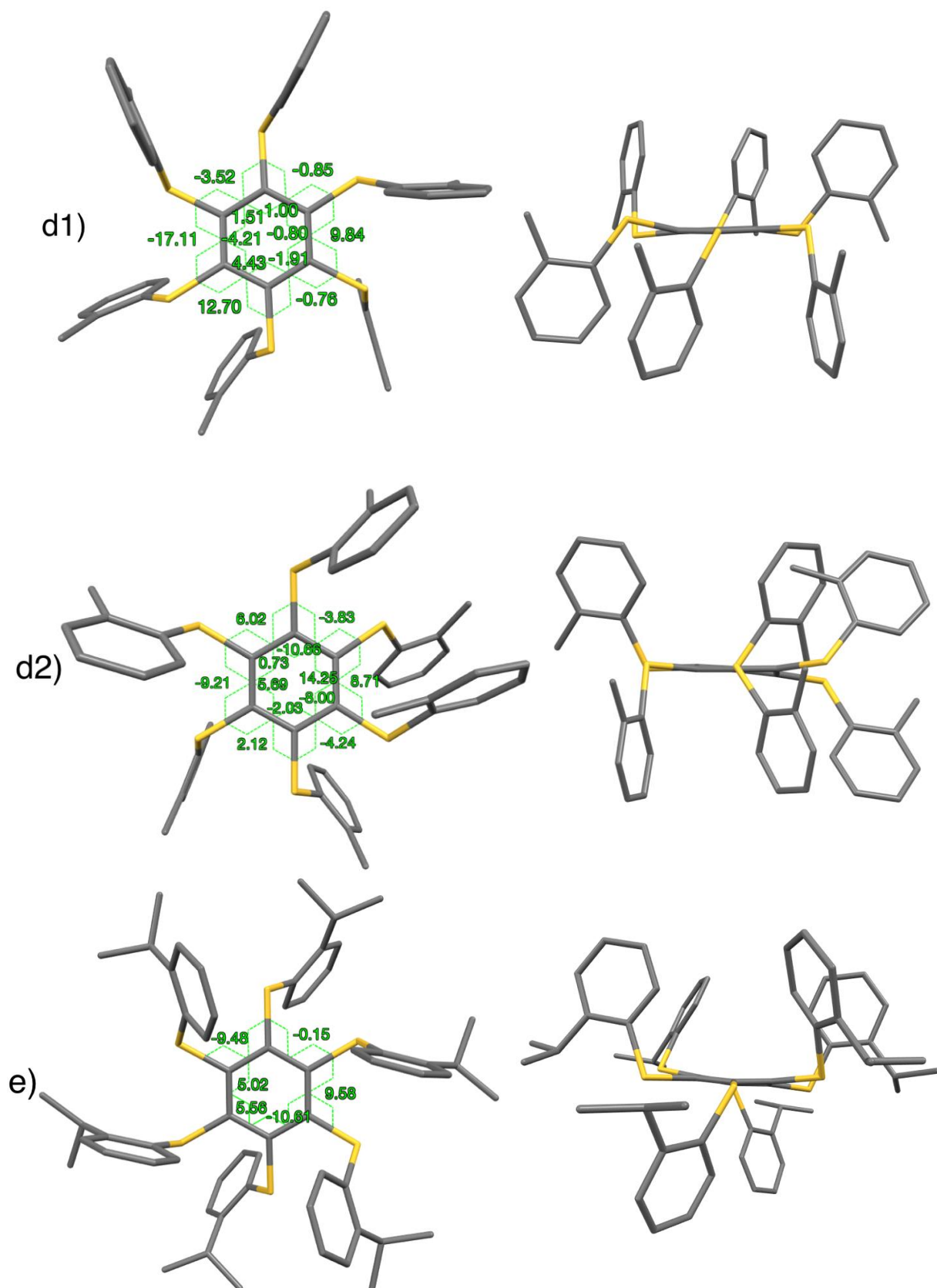


Figure S5. Torsion angles in degrees between core (CC-CC) and peripheral (SC-CS) bonds in crystals of **A6-oTol** (d1, *aaabbb* conformer; d2, *aabbab* conformer; data are taken from published results,^[3] CCDC refcode: GEGLAF). **A6-iPr** (e; see general information for CCDC data). Side views are also shown for each compound (right side). Hydrogen atoms are omitted for clarity.

DSC ANALYSIS

Differential scanning calorimetry (DSC) was performed on a PerkinElmer Pyris Diamond, equipped with a ULSP 90 intracooler, or on a DSC Q10 TA Instruments equipped with a RCS cooling system. Temperature and enthalpy calibrations were performed using high-purity standards (n-decane, benzene, and indium). Heating of the aluminum open pans containing the samples (3–5 mg) was carried out at 5 K/min in the selected temperature range (from 298 K to 473 K for heating cycles; from 473 K to 298 K for cooling cycles), under N₂ atmosphere, on powders and amorphous phases. The latter are obtained by the corresponding melted solids followed by fast quenching in liquid N₂.

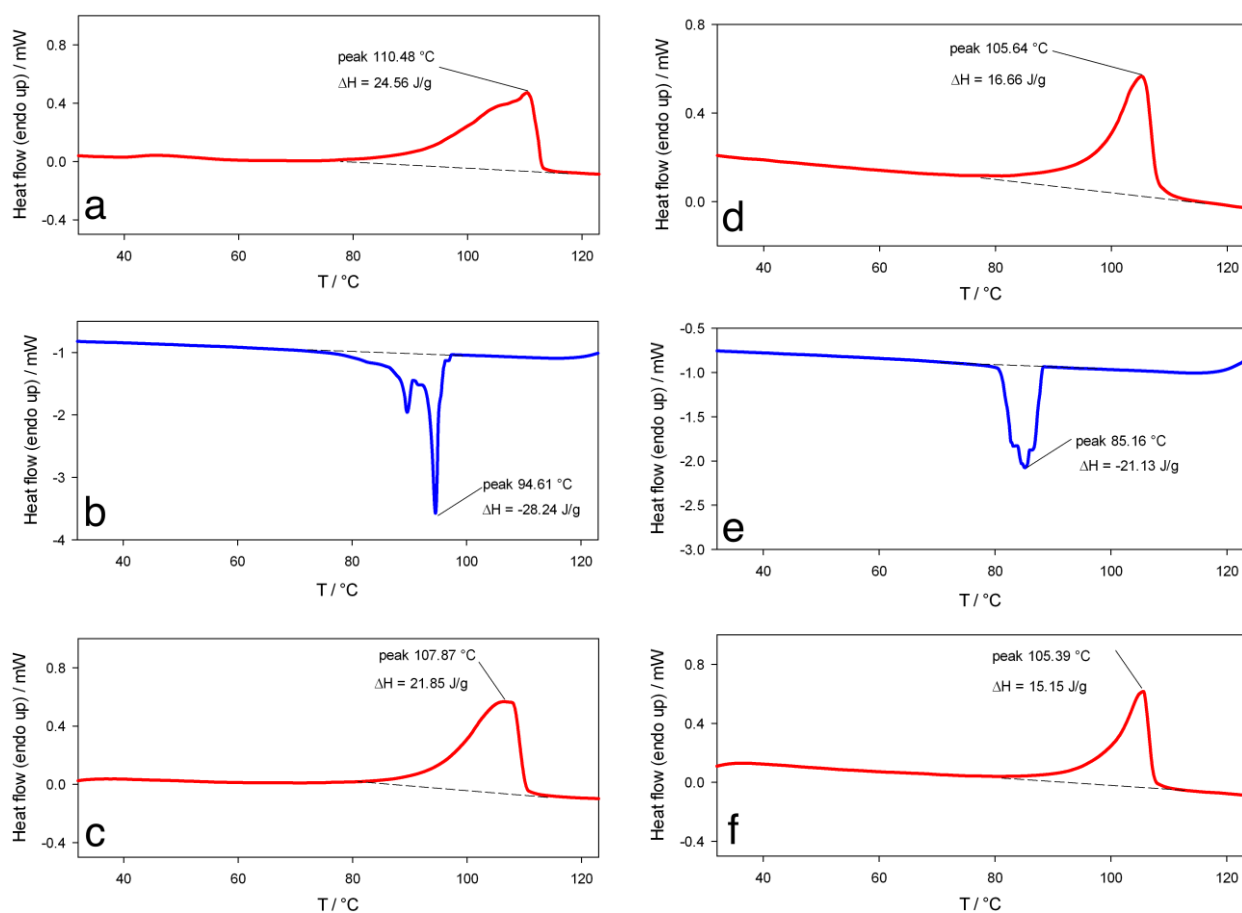


Figure S6. DSC traces obtained from crystalline sample of **B6-iPr** upon heating (a), cooling (b) and heating for a second cycle. The same heating-cooling-heating cycles (traces d, e, f) have been performed on an amorphous sample obtained after annealing of **B6-iPr**.

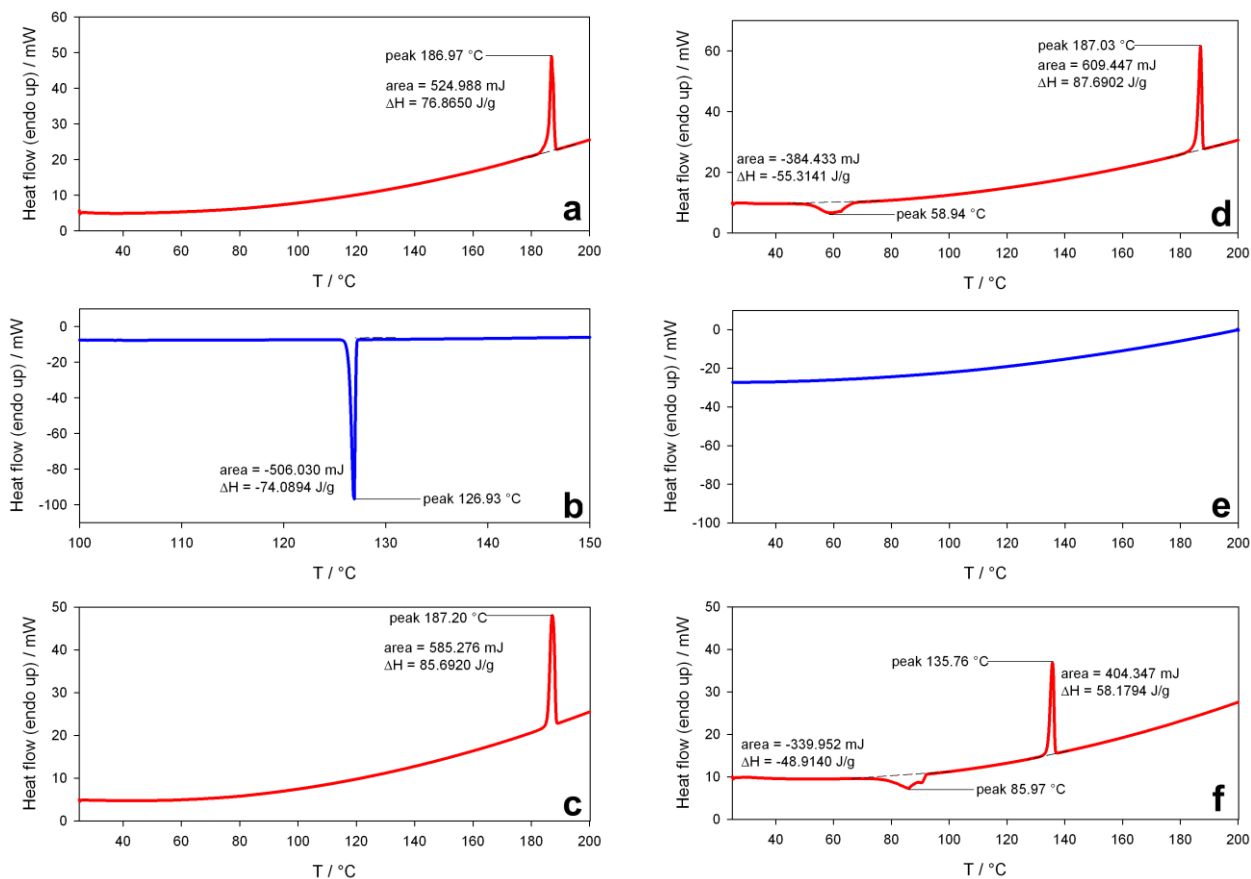


Figure S7. DSC traces obtained from crystalline sample of **A6-Ph** upon heating (a), cooling (b) and heating for a second cycle. The same heating-cooling-heating cycles (traces d, e, f) have been performed on an amorphous sample obtained after annealing of **A6-Ph**.

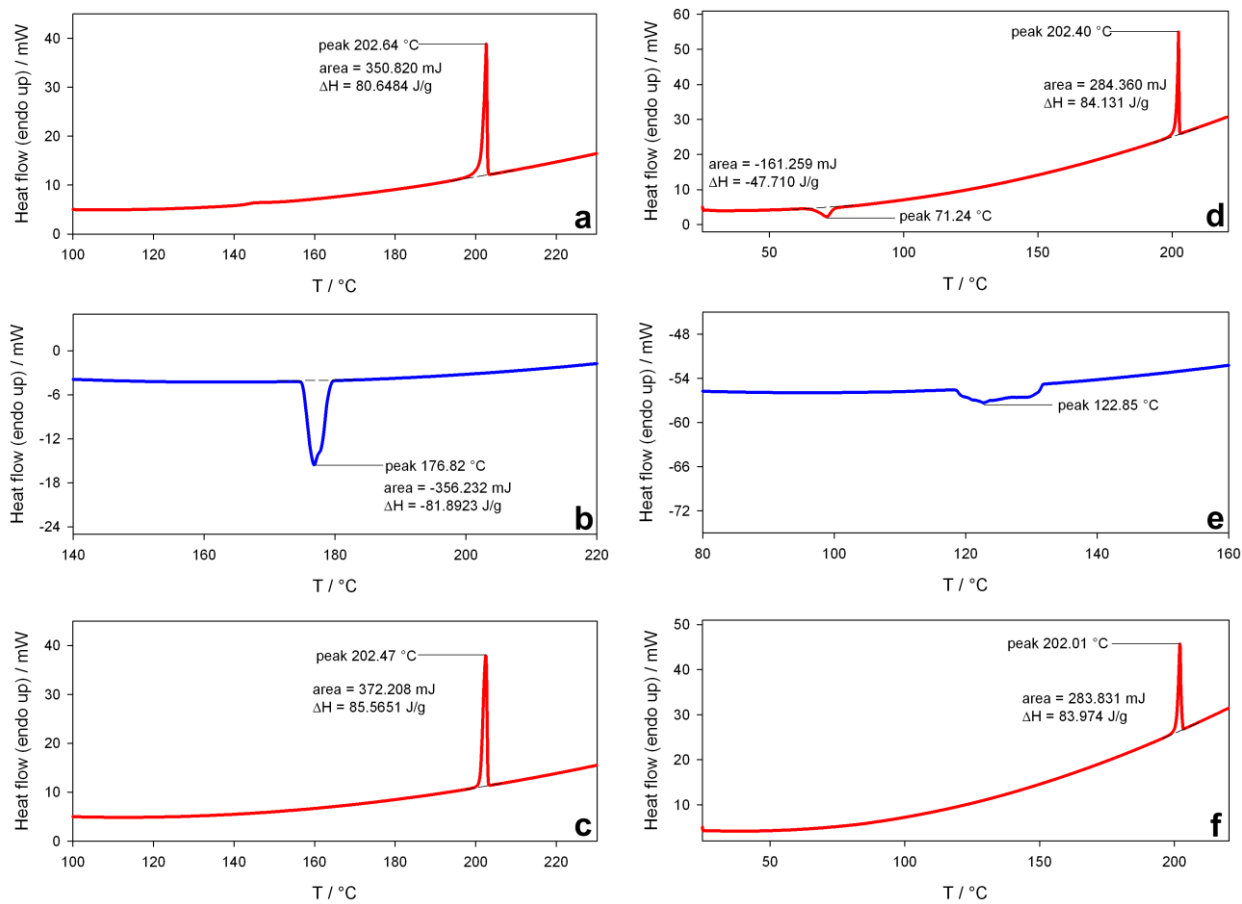


Figure S8. DSC traces obtained from crystalline sample of **A6-pTol** upon heating (a), cooling (b) and heating for a second cycle. The same heating-cooling-heating cycles (traces d, e, f) have been performed on an amorphous sample obtained after annealing of **A6-pTol**.

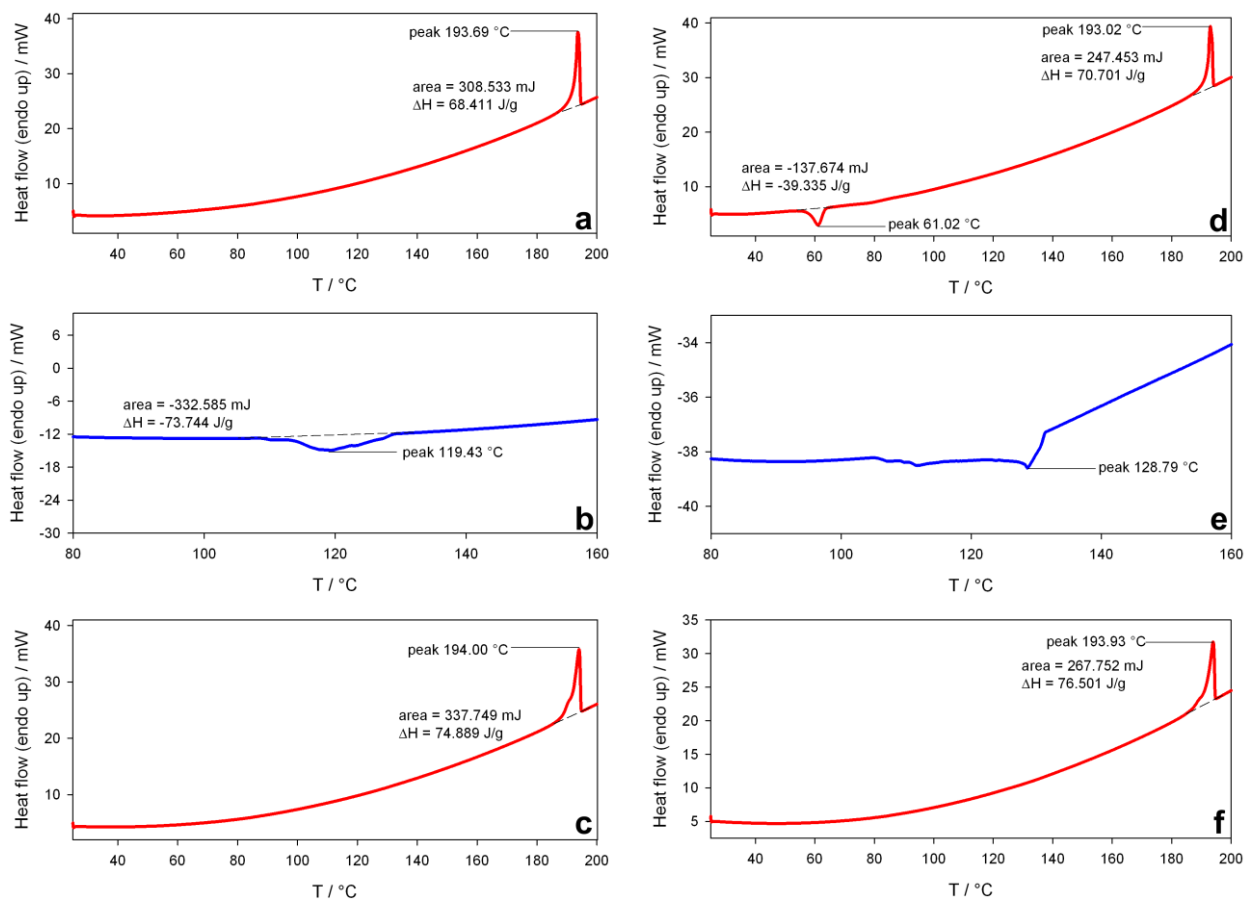


Figure S9. DSC traces obtained from crystalline sample of **A6-oTol** upon heating (a), cooling (b) and heating for a second cycle. The same heating-cooling-heating cycles (traces d, e, f) have been performed on an amorphous sample obtained after annealing of **A6-oTol**.

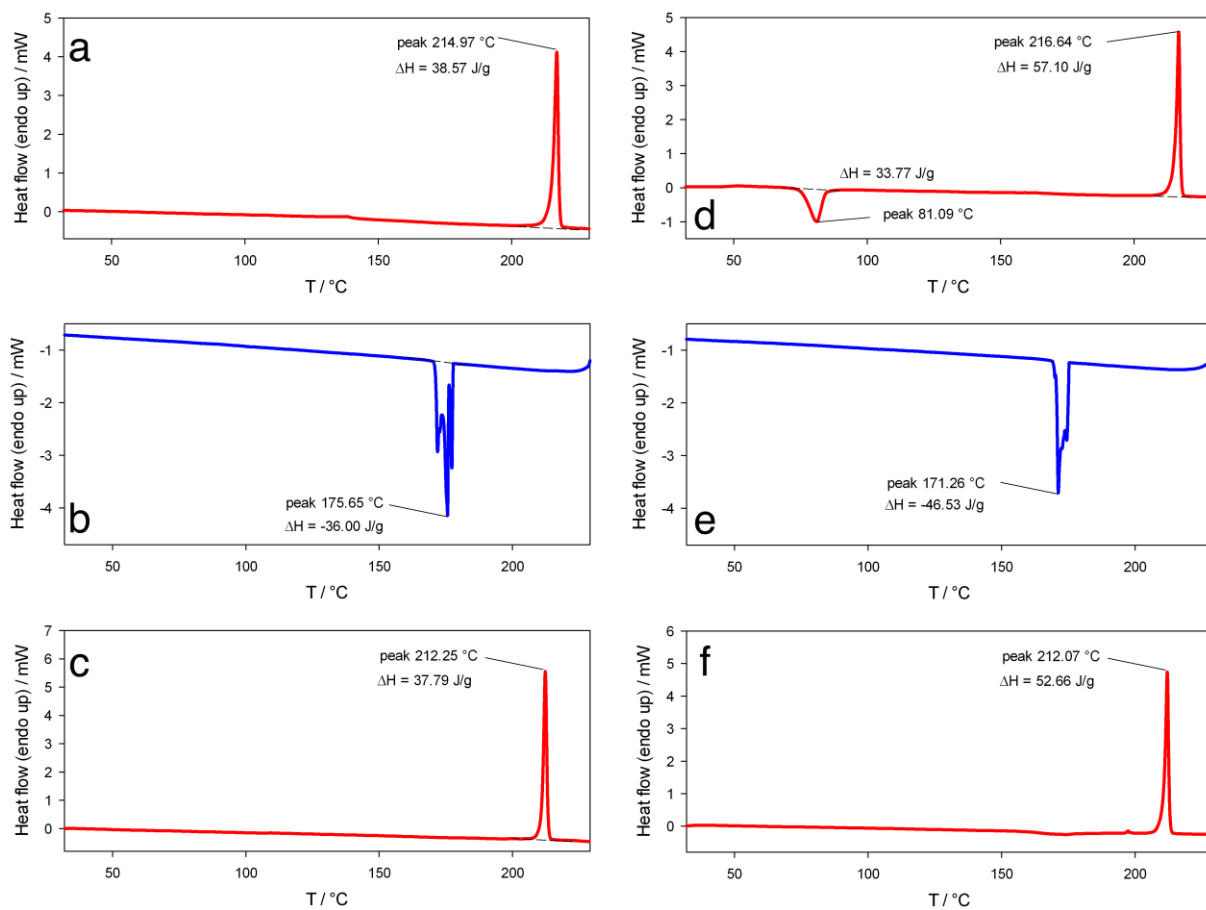


Figure S10. DSC traces obtained from crystalline sample of **A6-iPr** upon heating (a), cooling (b) and heating for a second cycle. The same heating-cooling-heating cycles (traces d, e, f) have been performed on an amorphous sample obtained after annealing of **A6-iPr**.

PHOTOPHYSICAL CHARACTERIZATION

All photophysical analyses were carried out in CH_2Cl_2 at 298 K, unless otherwise specified. UV–vis absorption spectra were recorded with a PerkinElmer $\lambda 40$ spectrophotometer using quartz cells with path length of 1.0 cm. Luminescence spectra and lifetimes were recorded and determined with a PerkinElmer LS-50, an Edinburgh FS5 or an Edinburgh FLS920 spectrofluorometer (equipped with a Hamamatsu Photomultiplier R928P phototube) or on a Varian Cary Eclipse phosphorimeter. Lifetimes shorter than 10 μs were measured by the same Edinburgh FLS920 spectrofluorometer by time-correlated single-photon counting (TCSPC) technique. Quantum yields are determined by means of an integrating sphere (LabSphere, 4 in. diameter) with the method developed by De Mello.^[9] Quantum yields at 77 K were calculated with the same apparatus using an homemade optical glass dewar flask, fitting the above-mentioned integrating sphere vertically. The estimated experimental errors are 2 nm on the band maximum, 5% on the molar absorption coefficient and luminescence lifetime and 20% on emission quantum yields.

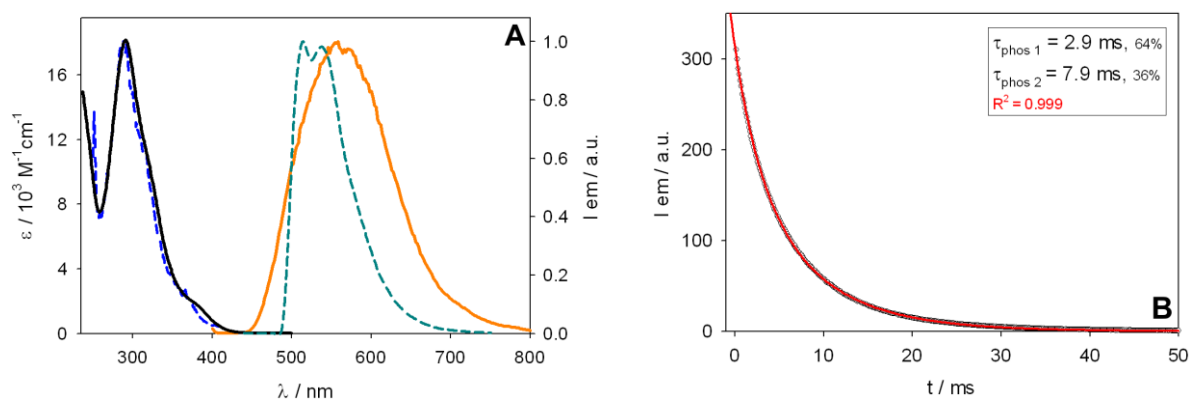


Figure S11. A: absorption (CH_2Cl_2 , rt; black line), emission ($\text{CH}_2\text{Cl}_2:\text{CH}_3\text{OH}$ 1:1 v/v, 77 K; orange line) and corresponding excitation spectrum (blue dashed line) for solutions of **B6-iPr**. The emission spectrum obtained from the crystalline phase at 77 K is also shown for comparison (green dashed line). $\lambda_{\text{ex}} = 390$ nm; $\lambda_{\text{em}} = 620$ nm. B: phosphorescence decays for a solution of **B6-iPr** in $\text{CH}_2\text{Cl}_2:\text{CH}_3\text{OH}$ 1:1 v/v at 77 K.

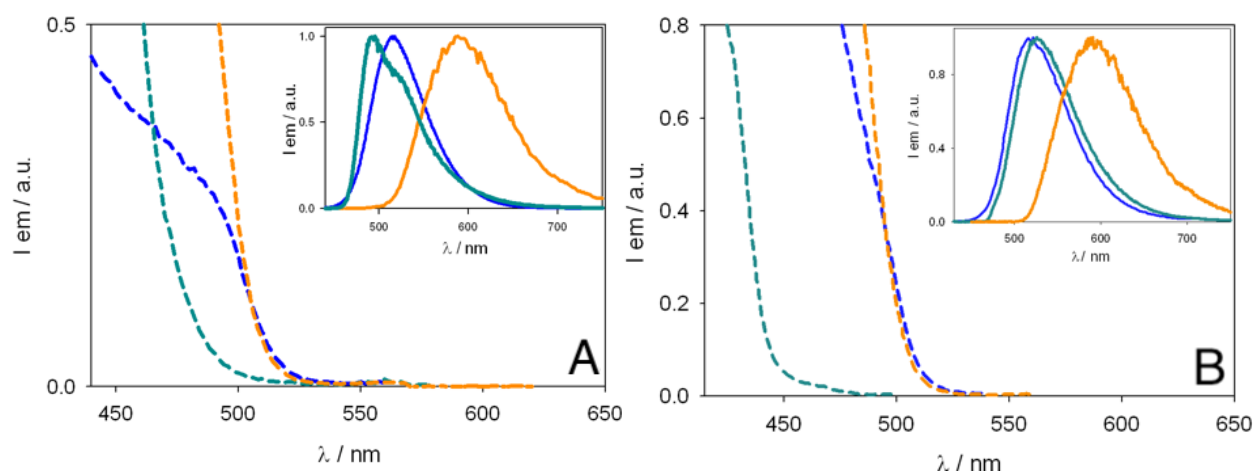


Figure S12. A: comparison between onsets of the excitation spectra obtained from crystalline (green dashed line: 77 K, $\lambda_{\text{em}} = 590$ nm; blue dashed line: RT, $\lambda_{\text{em}} = 580$ nm) and amorphous (dashed orange line: 77 K, $\lambda_{\text{em}} = 630$ nm) samples of **A6-pTol**. Inset: corresponding phosphorescence spectra obtained in the same experimental conditions. B: comparison between onsets of the excitation spectra obtained from crystalline (green dashed line: 77 K, $\lambda_{\text{em}} = 540$ nm) and amorphous (dashed orange line: 77 K, $\lambda_{\text{em}} = 630$ nm) samples of **A6-Ph**. Inset: corresponding phosphorescence spectra obtained in the same experimental conditions.

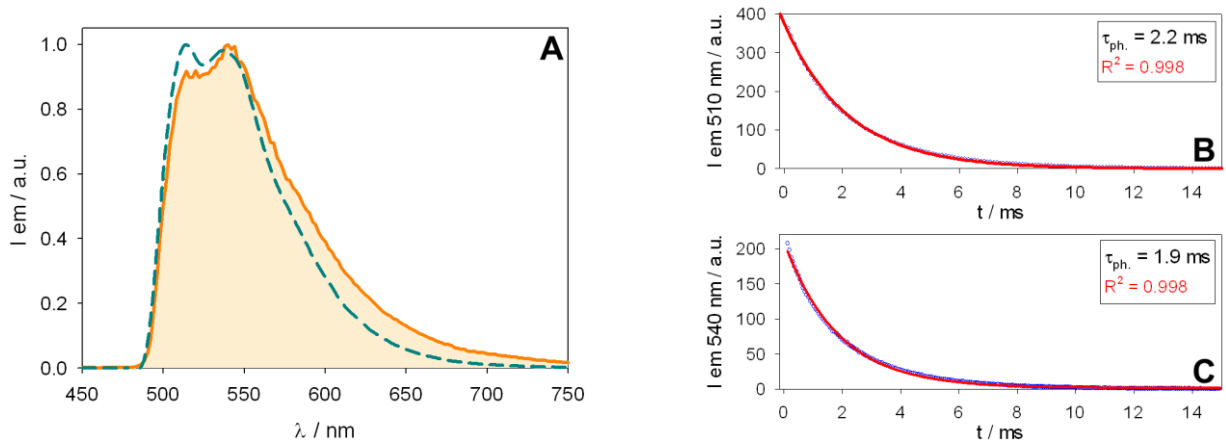


Figure S13. A: comparison between phosphorescence spectra at 77 K obtained for a crystalline sample of **B6-iPr** (green dashed line) and a sample obtained by fast cooling (in liquid N₂) of a melted phase (orange line). The corresponding emission decays are shown as insets B and C, respectively. $\lambda_{\text{ex}} = 350$ nm.

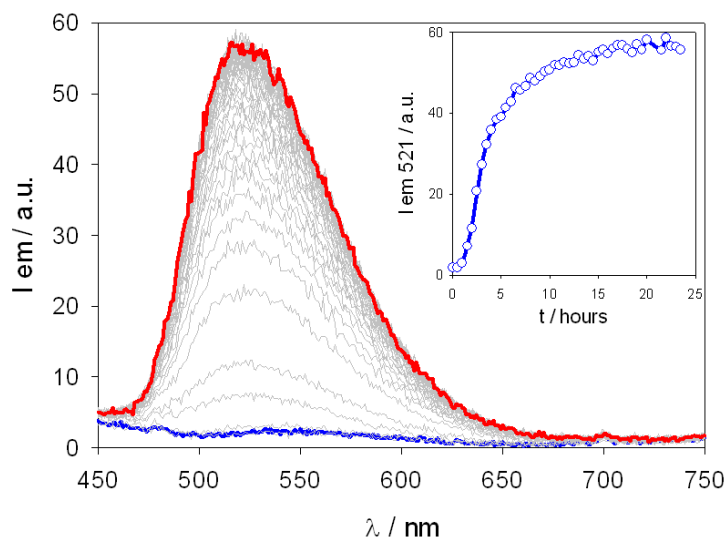


Figure S14. Emission profiles obtained at RT from the crystallization of an amorphous sample of **A6-Ph**. Inset: emission profile vs. time ($\lambda_{\text{ex}} = 521$ nm). $\lambda_{\text{ex}} = 360$ nm.

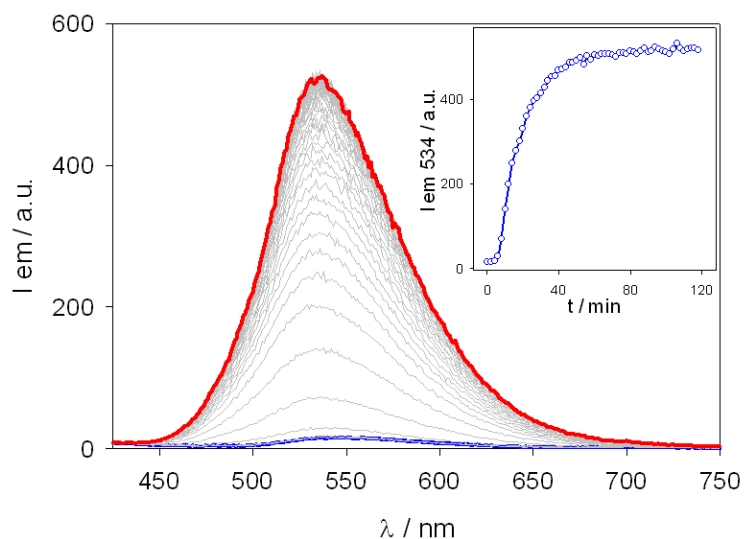


Figure S15. Emission profiles obtained at RT from the crystallization of an amorphous sample of **A6-pTol**. Inset: emission profile vs. time ($\lambda_{\text{ex}} = 534$ nm). $\lambda_{\text{ex}} = 360$ nm.

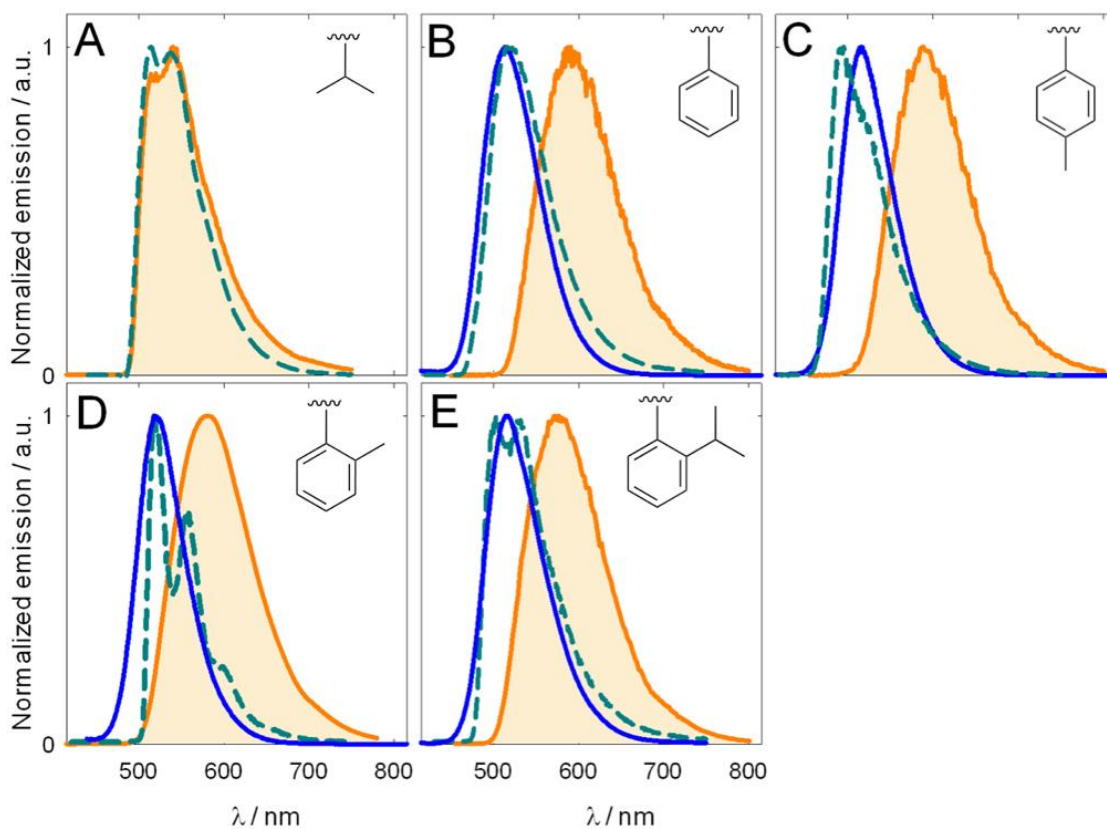


Figure S16. Comparison between normalized emission spectra of persulfurated benzenes **B6-iPr** (A) and **A6-** derivatives (B-F) recorded from crystalline phases at RT and at 77 K (blue and dashed green lines, respectively). Emission spectra for the corresponding solid amorphous phases at 77 K are also reported as orange lines. $340 < \lambda_{\text{ex}} < 380$ nm.

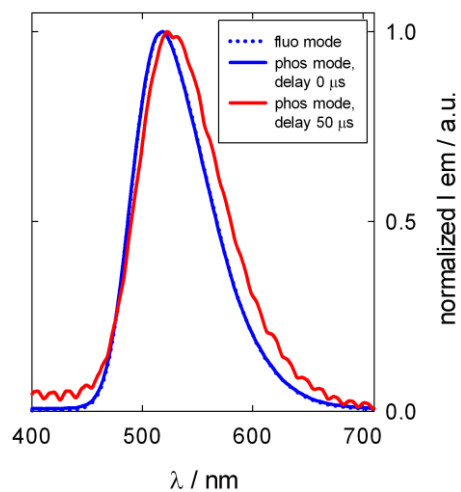


Figure S17. A: comparison between normalized emission spectra collected for solid **A6-pTol** at RT in steady-state (fluorescence mode) and time-gated acquisition at different delay times (0 - 50 μ s; phosphorescence mode). Gate time = 5 ms; λ_{ex} = 360 nm; excitation and emission slits are constants for all spectra recorded.

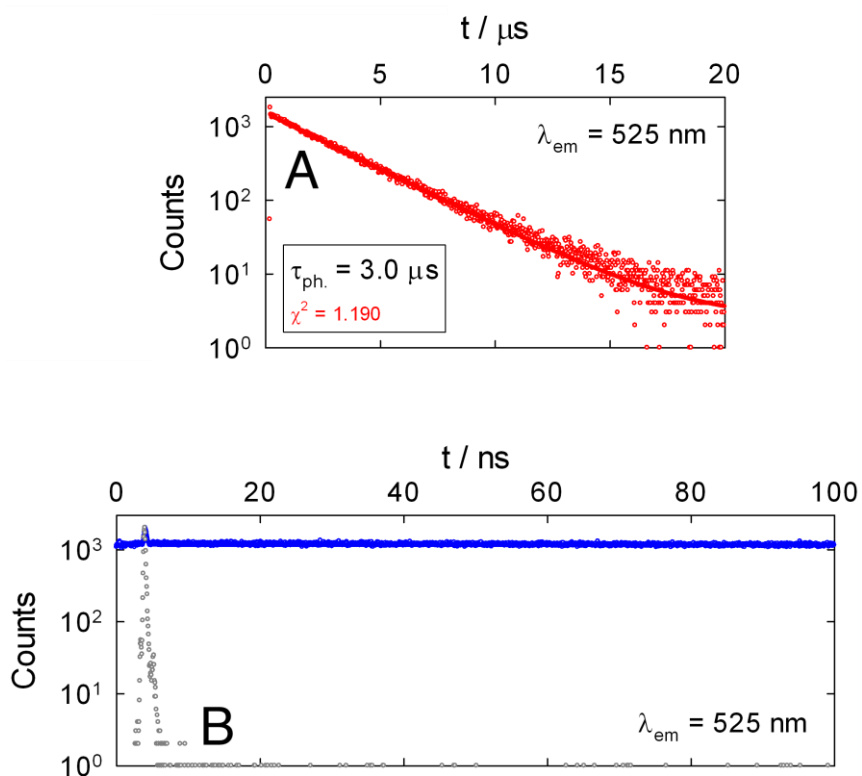


Figure S18. A-B: emission decays at $\lambda_{\text{em}} = 525$ nm for solid **A6-pTol** at RT and corresponding monoexponential fitting (time range = 20 μ s and 100 ns, respectively). $\lambda_{\text{ex}} = 405$ nm. The instrument response function is also shown in B (grey dots).

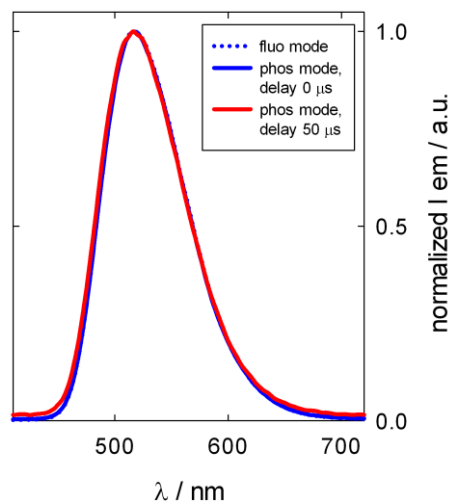


Figure S19. A: comparison between normalized emission spectra collected for solid **A6-Ph** at RT in steady-state (fluorescence mode) and time-gated acquisition at different delay times (0 - 50 μ s; phosphorescence mode). Gate time = 5 ms; λ_{ex} = 360 nm; excitation and emission slits are constants for all spectra recorded.

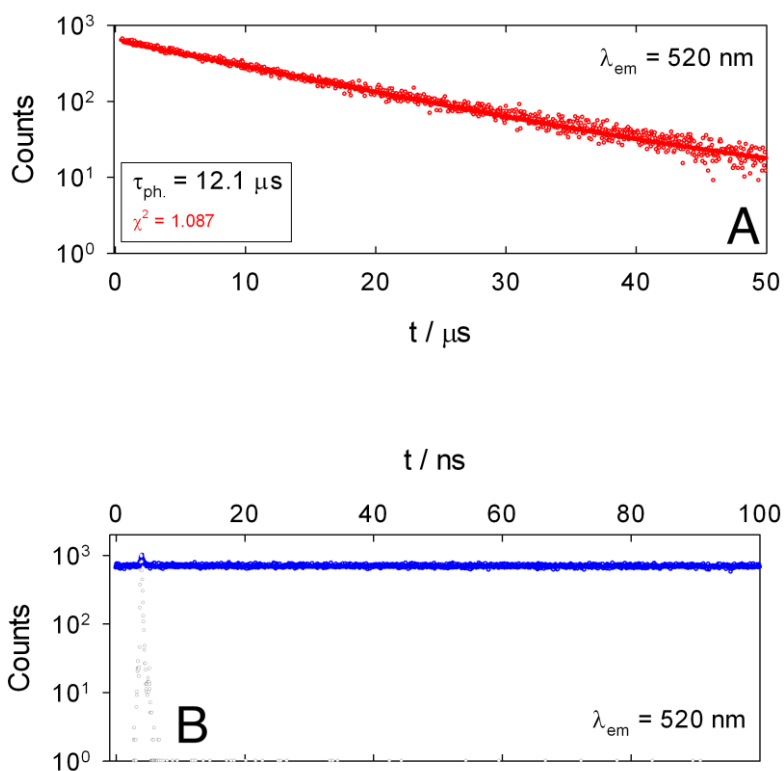


Figure S20. A-B: emission decays at $\lambda_{\text{em}} = 520$ nm for solid **A6-Ph** at RT and corresponding monoexponential fitting (time range = 50 μ s and 100 ns, respectively). $\lambda_{\text{ex}} = 405$ nm. The instrument response function is also shown in B (grey dots).

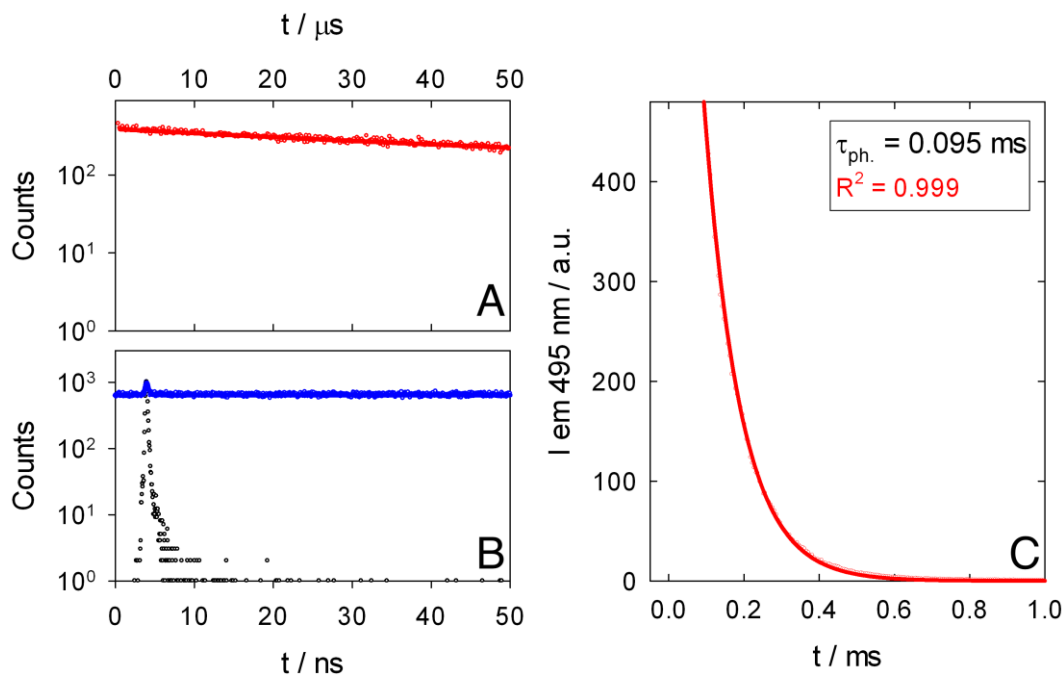


Figure S21. A-B: emission decays at $\lambda_{em} = 485$ nm for solid **A6-pTol** at 77 K and corresponding monoexponential fitting (time range = 50 μ s and 50 ns, respectively; $\lambda_{ex} = 405$ nm). The fitting of the decays obtained with these time ranges cannot be provided given the longer phosphorescence lifetimes. C: emission decay at $\lambda_{em} = 495$ nm for the same sample (time range = 1 ms; $\lambda_{ex} = 360$ nm). The instrument response function is also shown in B (grey dots).

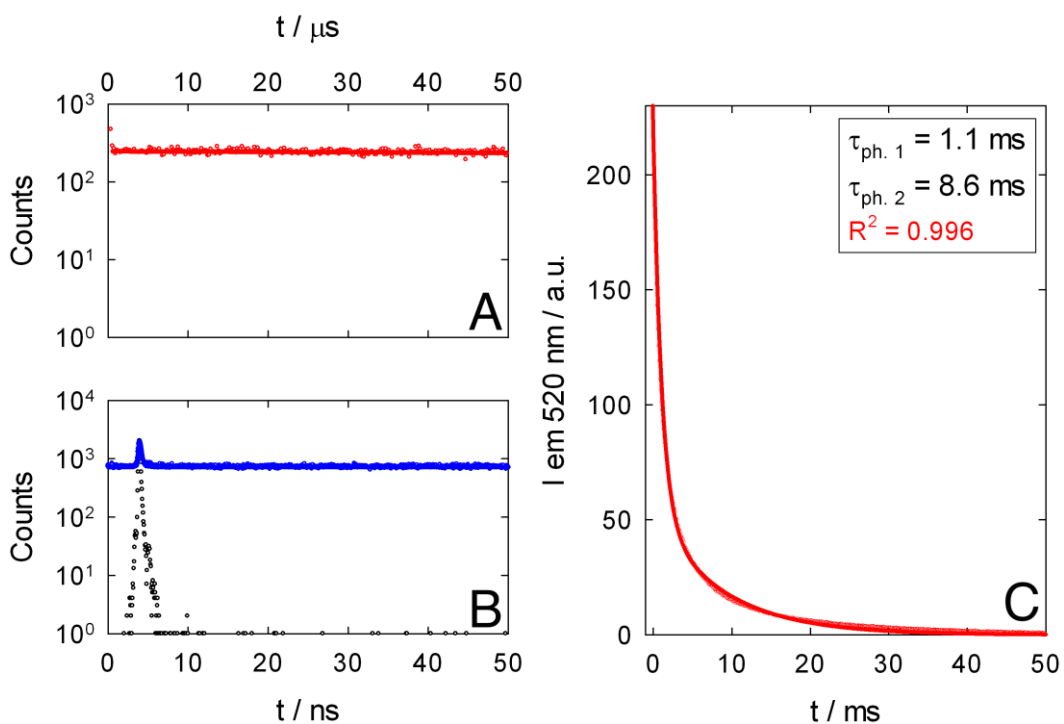


Figure S22. A-B: emission decays at $\lambda_{em} = 520$ nm for solid **A6-Ph** at 77 K and corresponding monoexponential fitting (time range = 50 μ s and 50 ns, respectively; $\lambda_{ex} = 405$ nm). C: emission decay at $\lambda_{em} = 520$ nm for the same sample (time range = 50 ms; $\lambda_{ex} = 360$ nm). The instrument response function is also shown in B (grey dots).

Table S2. Phosphorescence data for crystalline solid phases at 77 K.

Emission – crystalline phase at 77 K		
	λ_{max} (nm)	τ (ms)
B6-iPr	513	2.2
A6-Ph	516	1.1 – 8.6 ^a
A6-pTol	495	0.095
A6-oTol	518	0.6 – 2.3 ^a
A6-iPr	503	2.7 – 16.9 ^a

^a Biexponential fitting

COMPUTATIONAL DETAILS

The ground state geometries of **B6-iPr** and **A6-** derivatives were determined at M06-2X/def2-SVP level of theory including the D3 version of Grimme's dispersion.^[10] Vertical excitations energies were evaluated at TD-M06-2X level with the same basis set and D3 dispersion. Singlet excited state geometries were obtained at TD-M06-2X/def2-SVP + D3 level, while geometries of the lowest triplet states were optimized either with TD-M06-2X/def2-SVP +D3 or with UM06-2X/def2-SVP +D3.

A conformational analysis was carried out with CREST^[11] at GFN2-xTB level.^[12] Starting from the crystalline structure of **A6-Ph** we determined the optimized geometry of **A6-Ph** at GFN2-xTB level with the xTB program.^[13] The conformational search was performed with CREST using the default algorithm. 60 conformers were obtained and their ground state geometries were further optimized at M06-2X/def2-SVP+D3 level. After DFT optimization only 40 unique conformers were characterized by different absolute energies and HOMO/LUMO (H/L) gaps. To assess the effect of functionals on the relative stability of conformers, the forty conformers were reoptimized also at B3LYP/def2-SVP+D3BJ and at ω B97X-D/def2-SVP levels. A plot of the computed HOMO-LUMO gap for the different conformers (Figure S17) shows correlation between the computed stability of the conformer (in gas phase) and the H/L gap. The counterintuitive decrease of the HOMO-LUMO gap for more stable conformers can be rationalized by considering that stabilizing dispersion interactions between aryl substituents determine the stability of conformers but destabilize the energy of the HOMO, which is mainly localized on the persulfurated benzene core and is very sensitive to orientation of substituents (Figure S18). TDDFT calculations of excitation energies for selected conformers confirm the trend of the HOMO/LUMO gap, showing a decrease of the S_0/T_1 energy gap for more stable conformers (Table S5). However, the stability determined for isolated molecules may not be coincident to those in the condensed phase. For this reason molecular dynamics (MD) simulations were carried out (see below).

Spin-orbit coupling (SOC) integrals were calculated with the spin-orbit mean-field (SOMF) method, with one-center approximation applied to the exchange term, (SOMF(1X)).^[14,15] Relativistic corrections were included with the zeroth order regular approximation (ZORA)^[16] using the ZORA-def2-TZVP basis set. Excited state energies were determined at TDA-M06-2X level. The SOC calculations were carried out with ORCA 5.0.1,^[17] while all DFT and TDDFT calculations were performed using the Gaussian 16 suite of programs.^[18]

Two sets of MD simulations were carried out. The first set was carried out on a 5x5x5 supercell of the **A6-Ph** crystal with periodic boundary conditions and using the MM3 force field.^[19] We run a 1 ns molecular dynamics simulation, in the *NVT* ensemble at 300 K, using Berendsen's algorithm^[20] to simulate the presence of a thermal bath; the integration step was set to 1 fs. The second set of simulations was carried out to generate an amorphous sample of A6-Ph molecules. To this end 125 A6-Ph molecules were introduced randomly in a box using PACKMOL.^[21] The system was then equilibrated in the *NVT* ensemble at 300 K for 500 ps, followed by *NPT* equilibration at 300 K performed to converge the density. This was followed by a final a series of *NVT* runs performed on the 300 K equilibrated cell, in steps of decreasing temperatures (300-200-100-80 K) followed by a final 1ns simulation in the *NVT* ensemble at 80 K. All the simulations were performed with Tinker-8.10.2 *dynamic* subprogram.^[22]

From the equilibrated MD trajectories a few snapshots were extracted and used to run QM/MM calculations as follows. To assess the effect of the crystal/amorphous environment on photophysical properties we selected a molecule at the center of the simulation cell and optimized its ground state geometry with QM/MM calculations. This procedure was applied to several snapshots of equilibrated crystals or amorphous samples. At the optimized geometry we also computed the excitation energies of the central molecule surrounded by the crystal/amorphous environment, with QM/MM calculations. Vertical excitation energies were finally averaged over a few snapshots of MD. QM/MM calculations were performed with the Gaussian16 package and the ONIOM model,^[23] using the M06-2X functional

and def2-SVP basis set for the high-level region (i.e. a central **A6-Ph** molecule) and the QM calculations included electronic embedding. The low-level region (molecular mechanics) was modelled by atomic point charges determined by the charge equilibration (Qeq) approach^[24] using the Dreiding force field^[25] parameters attributed to the fixed molecular geometry of the surrounding **A6-Ph** molecules. In addition, a QM/MM geometry optimization of the lowest triplet excited state of the central **A6-Ph** molecule was carried out within the crystal environment to assess the effect of restricted internal motions forced by the rigid environment on geometry changes upon excitation and their effects on computed excitation energies.

Table S3. Computed SOC's with the spin-orbit mean-field (SOMF) method. Excited state energies were determined at TDA-M06-2X level using the ZORA-def2-TZVP basis set.

@ geo triplet $n\pi^*$	
conformer	$T_1 = n\pi^*$
	$\langle T_1 \widehat{H}_{SOC} S_0 \rangle / \text{cm}^{-1}$
A6-Ph - <i>ababab</i>	0
A6-Ph - <i>aaabbb</i>	0
B6-iPr - <i>ababab</i>	0
@ geo triplet $\pi\pi^*$	
conformer	$T_1 = \pi\pi^*$
	$\langle T_1 \widehat{H}_{SOC} S_0 \rangle / \text{cm}^{-1}$
A6-Ph - <i>ababab</i>	0
A6-Ph - <i>aabaab</i>	24.2
B6-iPr - <i>ababab</i>	0

Table S4. Absolute energies (a.u.) of the optimized ground and triplet excited states of molecules / conformers studied in this work. M06-2X and TD-M06-2X calculations using the def2-SVP basis set and D3 dispersion correction.

Conformers	S_0	$T (n\pi^*)$	$T (\pi\pi^*)$
B6-iPr - <i>ababab</i>	-3327.038815	-3326.926155	-3326.930566
A6-Ph - <i>ababab</i>	-4005.007465	-4004.913209	-4004.905464
A6-Ph - <i>aaabbb</i>	-4005.01757	-4004.918628	/
A6-Ph - <i>aabaab</i>	-4005.016169	/	-4004.926229
A6-Ph - <i>aaabab</i>	-4005.01262	-4004.913291	-4004.927021

Table S5. Computed excitation energies (eV) at the optimized ground state of selected **A6-Ph** conformers. From TD-M06-2X/def2-SVP calculations supplemented with the D3 dispersion correction.

Conformer	S ₁ (nπ*) ^a / eV	T ₁ / eV	T ₂ / eV
<i>ababab</i>	3.80	3.26 (ππ*) ^a	3.59 (nπ*) ^a
<i>aaabbb</i>	3.35	3.05 (nπ*) ^a	3.67 (ππ*) ^a
<i>aaaabb(I)</i>	3.34	2.99 (nπ*) ^a	3.57 (ππ*) ^a
<i>aaaabb(II)</i>	3.30	2.99 (nπ*) ^a	3.57 (ππ*) ^a
<i>aaabab</i>	3.31	3.18 (nπ*) ^a	3.65 (ππ*) ^a
<i>aaaaab</i>	3.42	3.11 (nπ*) ^a	3.50 (ππ*) ^a
<i>aabaab</i>	3.81	3.11 (ππ*) ^a	3.50 (nπ*) ^a

^aThe dominant character of the excited state.

Table S6. TD-M06-2X/def2-SVP computed excitation energies (E / eV) of the lowest triplet and singlet excited states of an **A6-Ph** molecule, *ababab* conformer, embedded in the crystal environment at 300 K or in the amorphous environment at 80 K (from MD simulations)

Excited state	Crystal MD 300K E / eV	Amorphous MD 80 K E / eV	Gas phase E / eV
T ₁	3.20	3.03	3.59
S ₁	3.33	3.48	3.80

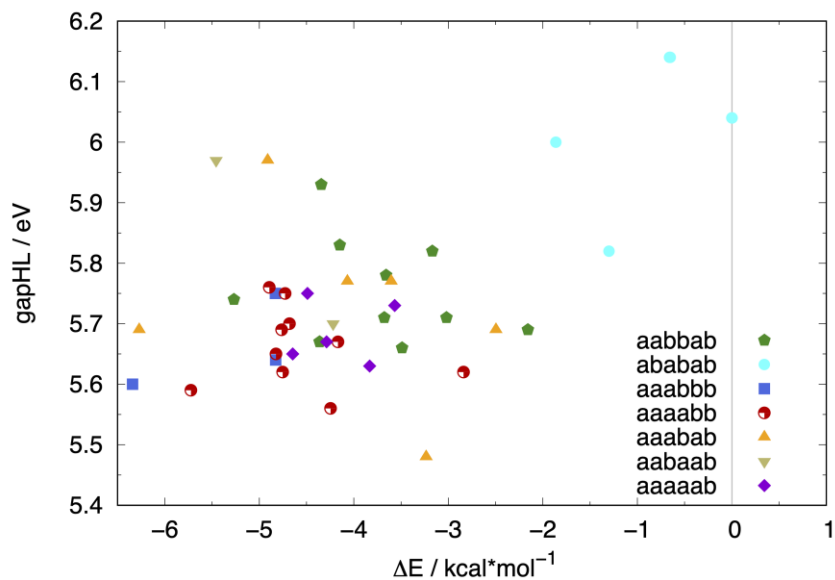


Figure S23. Computed HOMO-LUMO gap for the ground state optimized geometries (M06-2X/def2SVP+D3), determined through conformational analysis and plotted with respect to the relative energy of the symmetric *ababab* found in the crystal structure of **A6-Ph**. Each color identifies different conformers; points plotted with the same color represent different geometries calculated within the same conformer subset.

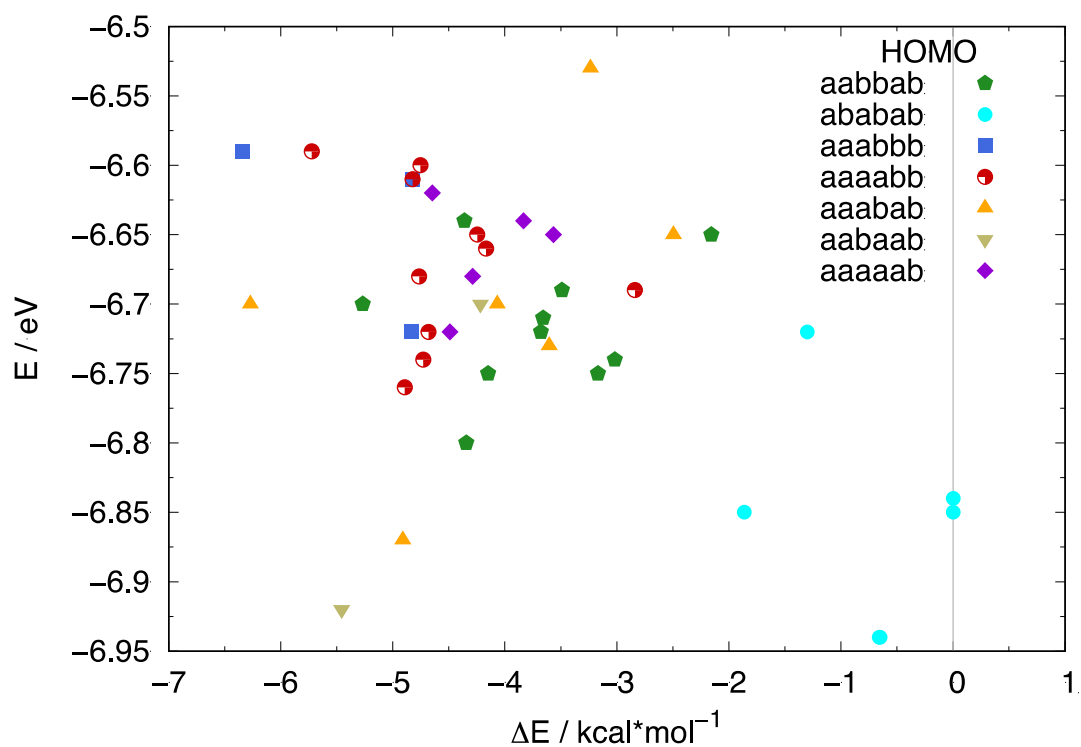


Figure S24. A6-Ph: computed HOMO energy at the ground state optimized geometry (M06-2X/def2SVP) of the conformers determined through conformational analysis, plotted with respect to the relative energy of the symmetric *ababab* found in the crystal structure of **A6-Ph**. Each color identifies different conformers; points plotted with the same color represent different geometries calculated within the same conformer subset.

- continued -

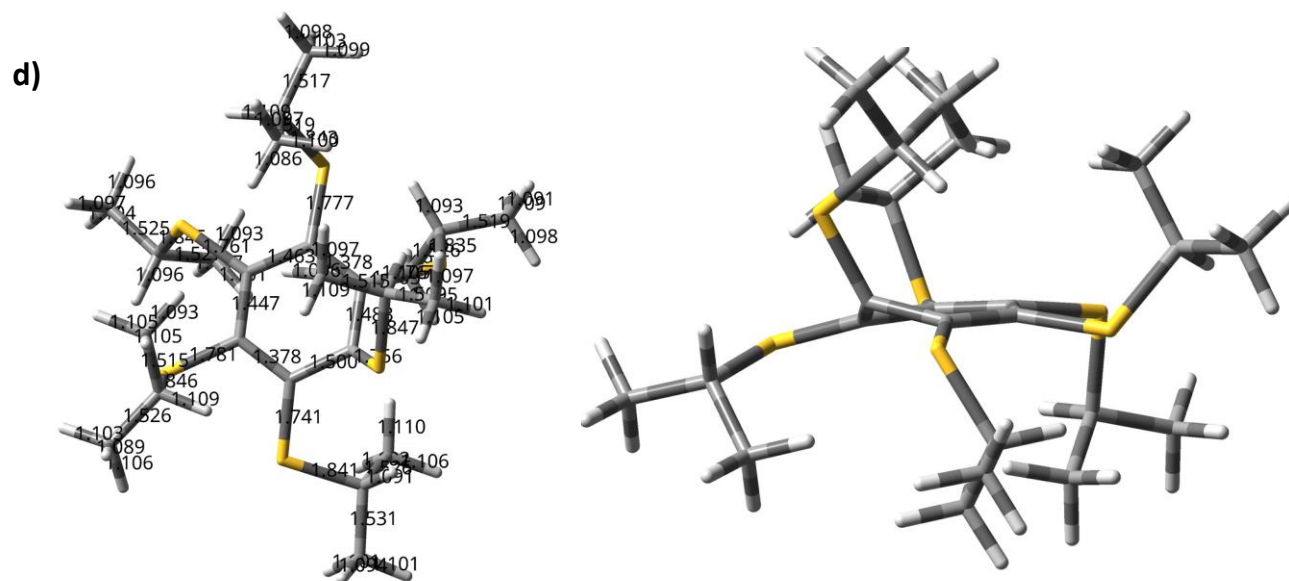


Figure S25. B6-iPr, *ababab* conformer: Optimized geometries of a) the ground (M06-2X/def2-SVP), b) the lowest triplet excited state with $\pi\pi^*$ character (TD-M06-2X/def2-SVP), c) the lowest triplet state with $\pi\pi^*$ character (TD-M06-2X/def2-SVP) determined only with a symmetry constraint and d) geometry of the T_1/S_0 crossing point, found during geometry optimization of the lowest triplet excited state with $\pi\pi^*$ character without symmetry constraint (TD-M06-2X/def2-SVP).

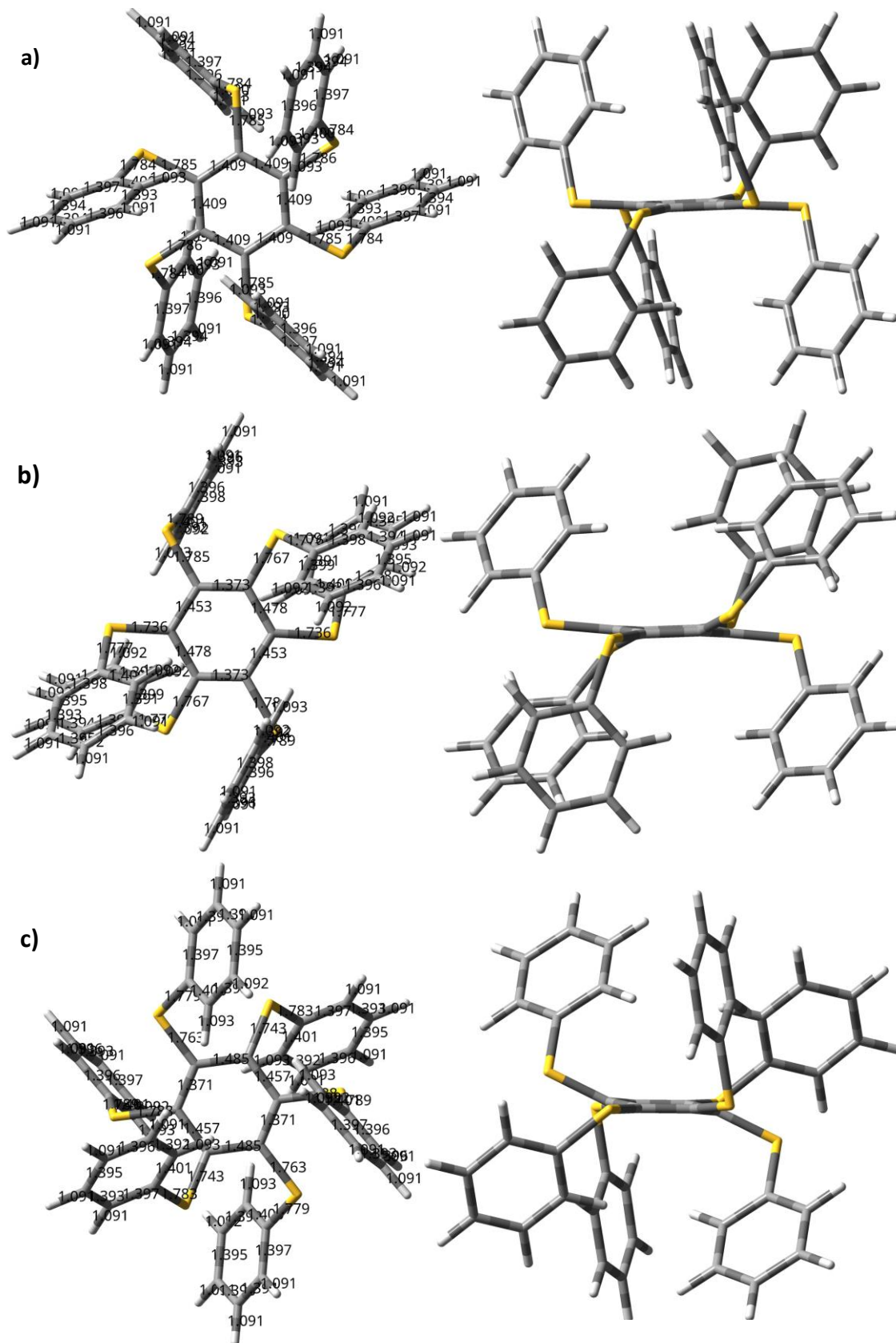


Figure S26. A6-Ph, *ababab* conformer: Optimized geometries of a) the ground (M06-2X/def2-SVP), b) the lowest triplet excited state with dominant $\pi\pi^*$ character (TD-M06-2X/def2-SVP) and c) the lowest triplet state with dominant $\pi\pi^*$ character (TD-M06-2X/def2-SVP).

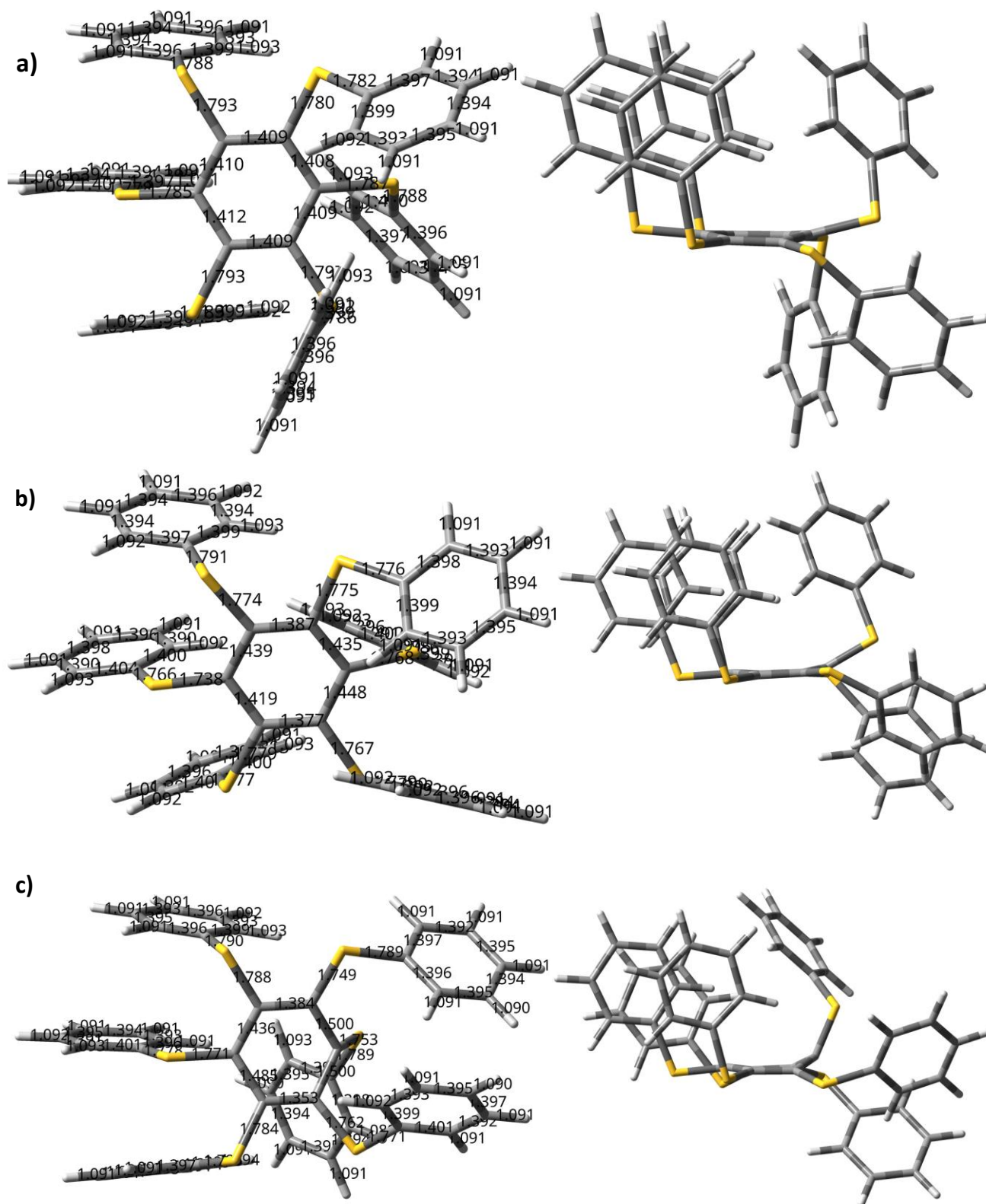


Figure S27. A6-Ph, *aaabab* conformer: Optimized geometries of a) the ground (M06-2X/def2-SVP), b) the lowest triplet excited state with $n\pi^*$ character (UM06-2X/def2-SVP) and c) geometry of the T_1/S_0 crossing point, found during geometry optimization of the lowest triplet excited state with $\pi\pi^*$ character (TD-M06-2X/def2-SVP).

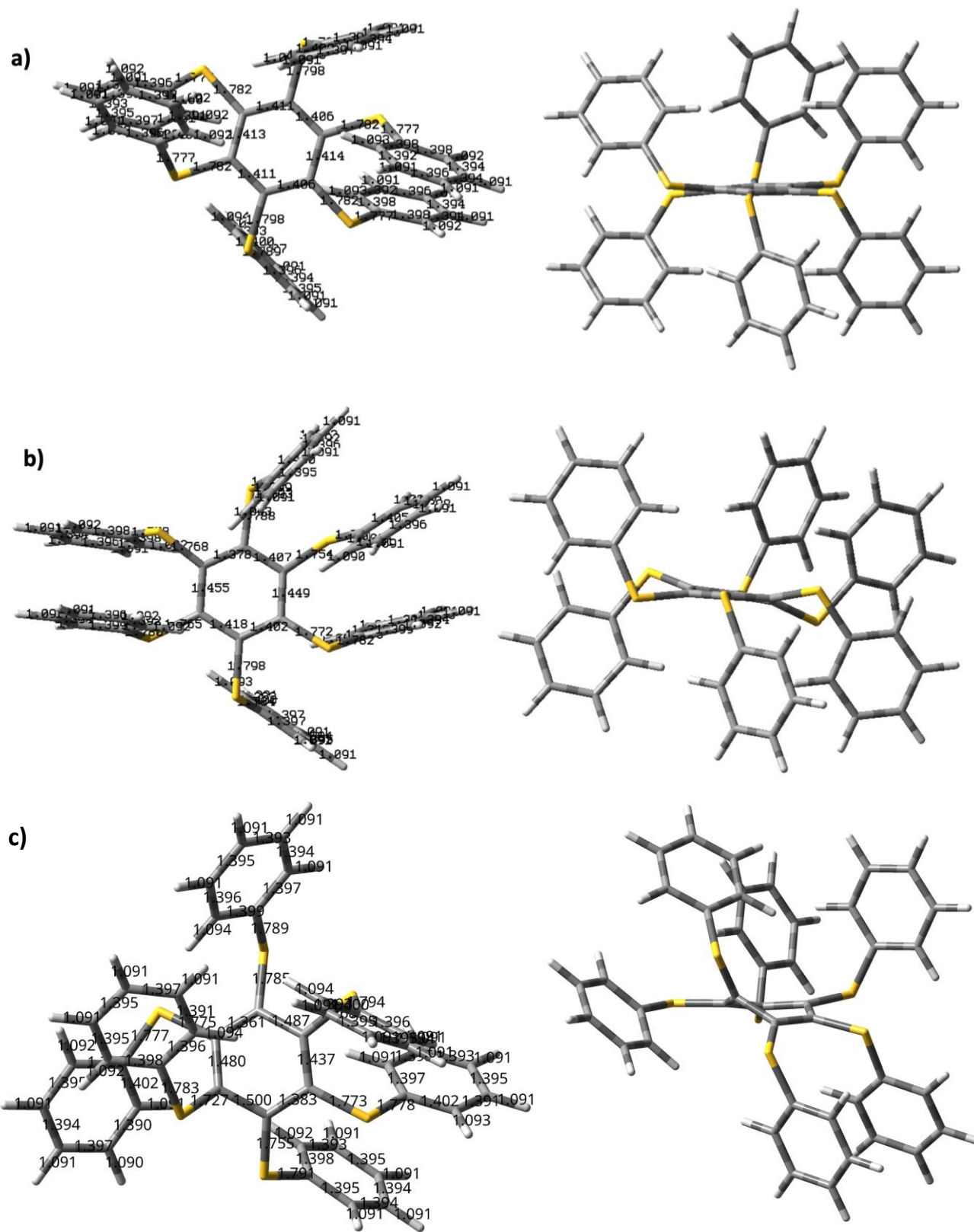


Figure S30. A6-Ph, *aabbab* conformer: Optimized geometries of a) the ground (M06-2X/def2-SVP), b) the lowest triplet excited state with dominant $n\pi^*$ character (UM06-2X/def2-SVP) and c) geometry of the T_1/S_0 crossing point, found during geometry optimization of the lowest triplet excited state with $\pi\pi^*$ character (TD-M06-2X/def2-SVP).

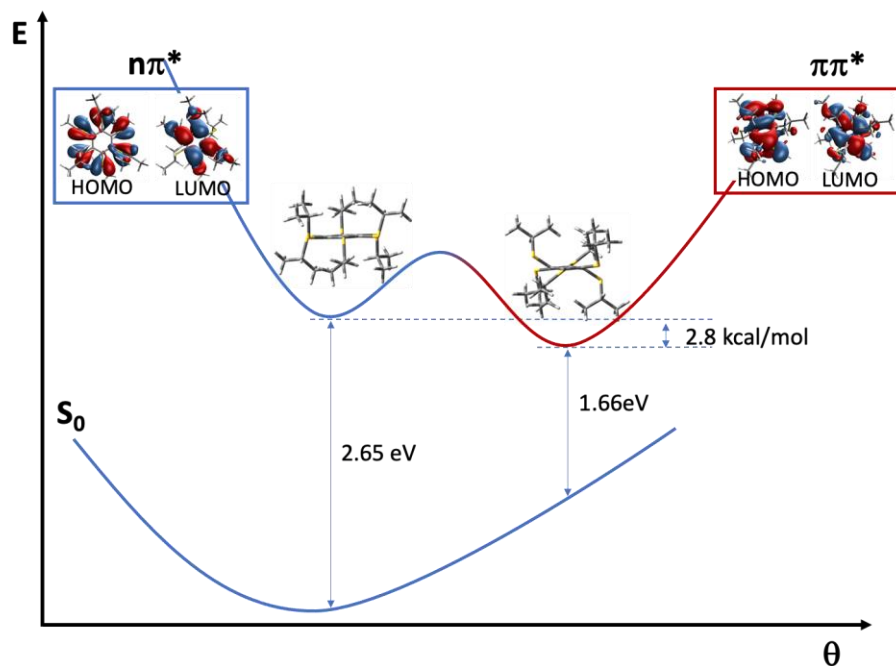


Figure S31. B6-iPr, *ababab* conformer under symmetry constraint: schematic representation of the potential energy profiles of the two lowest triplet excited states (TD-M06-2X/def2-SVP) and of the ground state (M06-2X/def2-SVP). θ is a displacement coordinate representing the multidimensional distortion of the central core as evidenced by the two optimized structures.

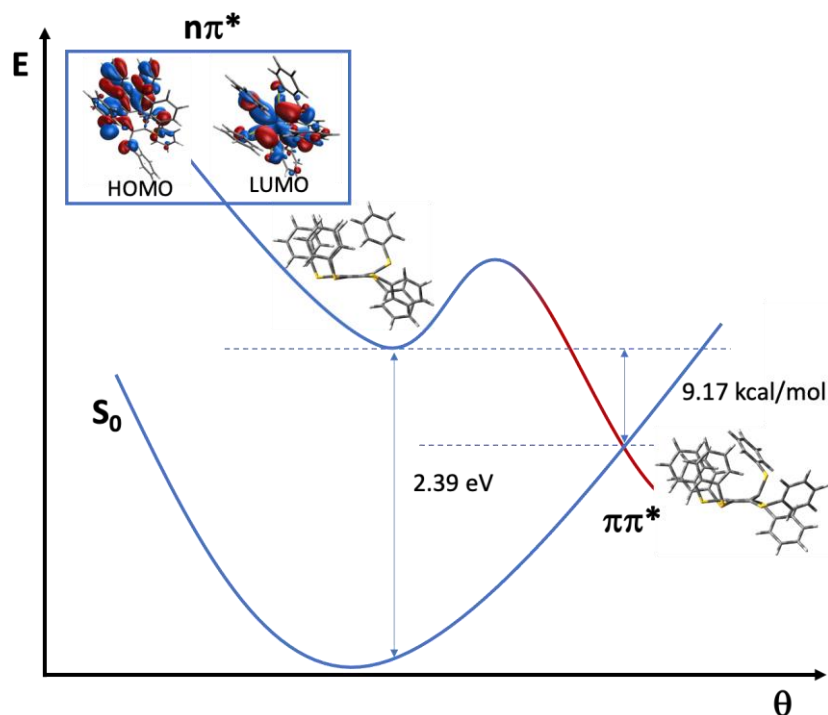


Figure S32. A6-Ph *aaabab* conformer. Schematic representation of the potential energy profiles of the two lowest triplet excited states (blue: $n\pi^*$ (UM06-2X/def2-SVP), red: $\pi\pi^*$ (TD-M06-2X/def2-SVP)) and of the ground state (M06-2X/def2-SVP). θ is a displacement coordinate representing the multidimensional distortion of the central core as evidenced by the two optimized structures (the triplet minimum and T_1/S_0 crossing point).

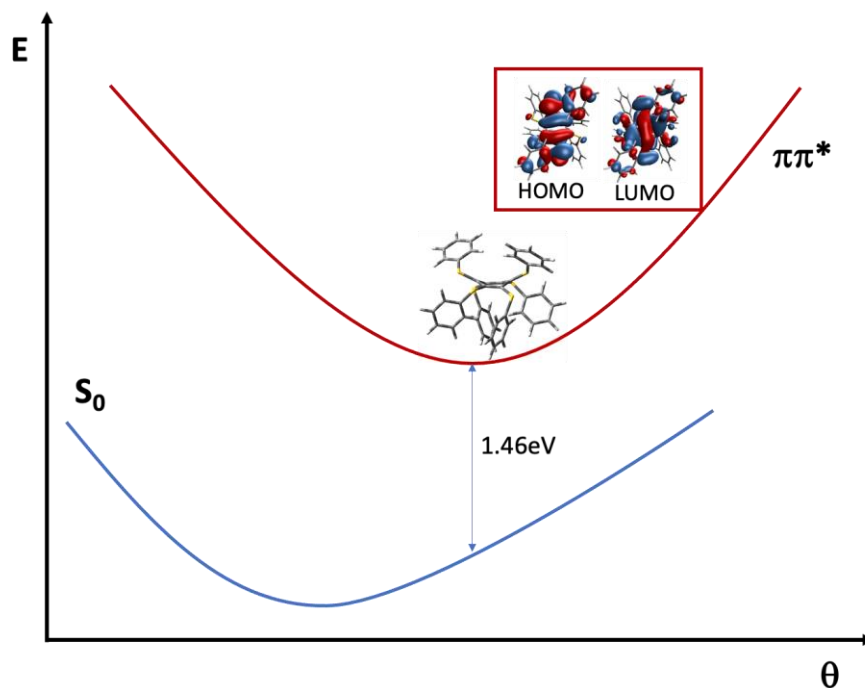


Figure S33. A6-Ph *aabaab* conformer. Schematic representation of the potential energy profiles of the lowest triplet excited state (TD-M06-2X/def2-SVP) and of the ground state (M06-2X/def2-SVP). θ is a displacement coordinate representing the multidimensional distortion of the central core.

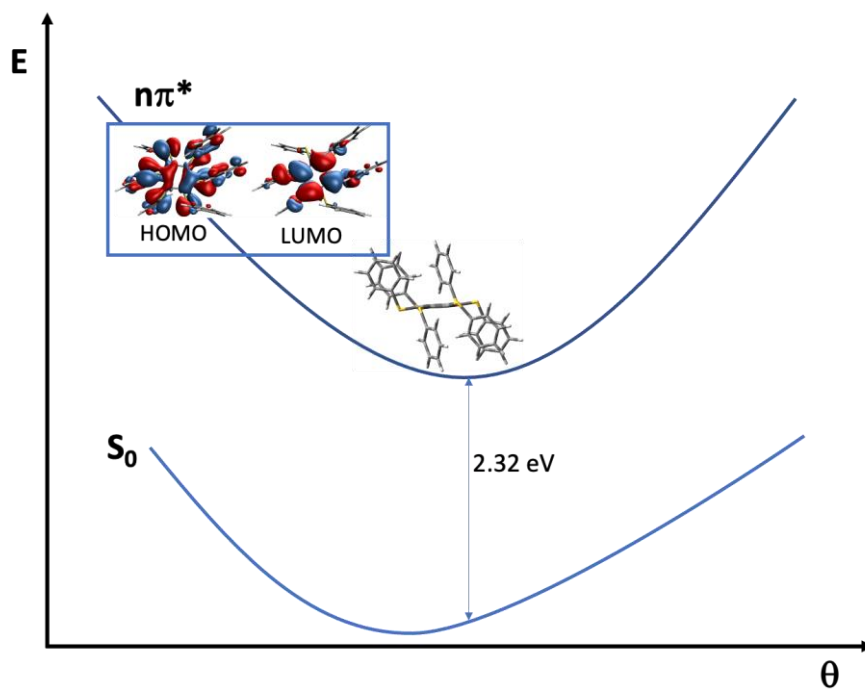


Figure S34. A6-Ph *aaabbb* conformer. Schematic representation of the potential energy profiles of the lowest triplet excited state (TD-M06-2X/def2-SVP) and of the ground state (M06-2X/def2-SVP). θ is a displacement coordinate representing the multidimensional distortion of the central core.

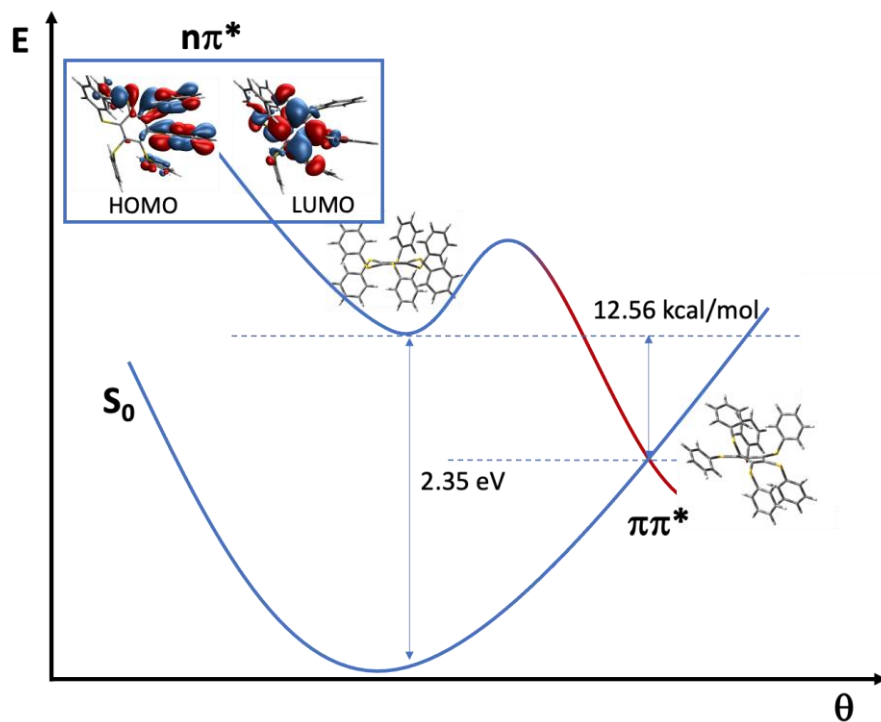


Figure S35. A6-Ph *aabbab* conformer. Schematic representation of the potential energy profiles of the lowest triplet excited states ((blue: $n\pi^*$ (UM06-2X/def2-SVP), red: $\pi\pi^*$ (TD-M06-2X/def2-SVP)) and of the ground state (M06-2X/def2-SVP). θ is a displacement coordinate representing the multidimensional distortion of the central core as evidenced by the two optimized structures (the triplet minimum and T_1/S_0 crossing point).

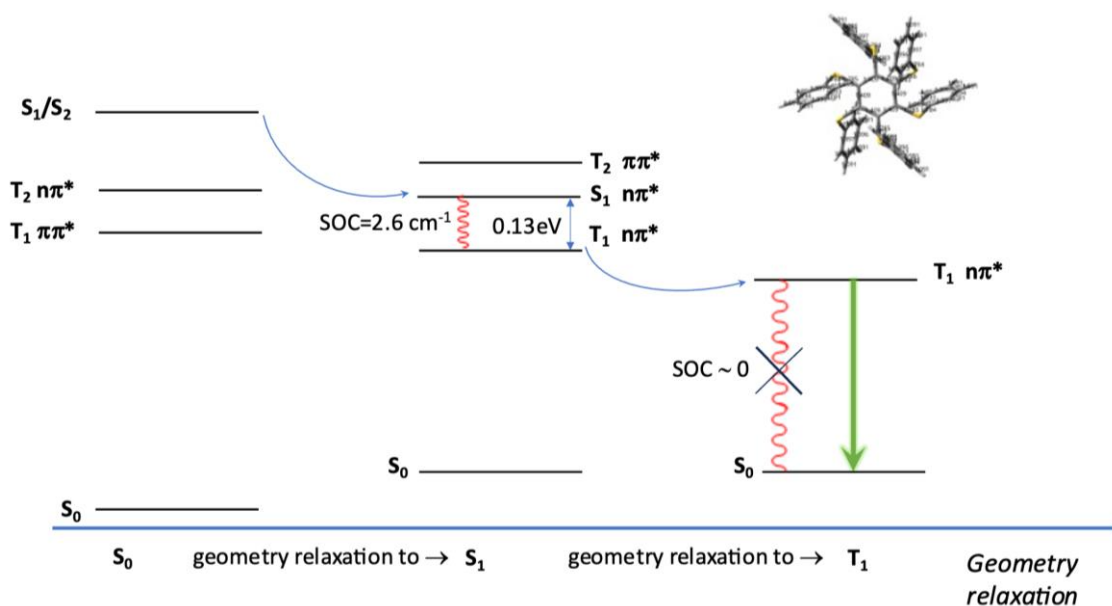
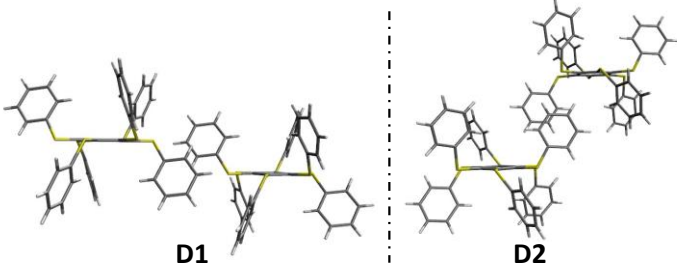


Figure S36. Schematic representation of the photoinduced processes leading to phosphorescence in A6-Ph *ababab* conformer. The magnitude of relevant energy differences (in eV) and SOCs (in cm^{-1}) are indicated.

Table S7. A6-Ph *ababab* conformer: excitation energies of the first two excited triplet states of the monomer along with the first four exciton states of two different dimers (**D1** and **D2**) extracted from the crystal structure. The subscript D in ‘Wavefunction’ indicates molecular orbitals of the dimer. T₁ and T₂ states of both dimers are generated from the T₁ state of the monomer; T₃ and T₄ states of the dimers are generated from the monomer’s T₂ state. TD-M06-2X/def2-SVP +D3 calculations.



Excited state in <i>ababab</i> monomer			
State	Exc. Energy/eV	Wavefunction	Nature
T ₁	3.19	0.46 H-1 → L+1	$\pi\pi^*$
		0.35 H-3 → L	
T ₂	3.43	0.57 H → L	$n\pi^*$
Exciton state in <i>ababab</i> dimer (D1)			
State	Exc. Energy/eV	Wavefunction	Nature
T ₁	3.19	0.32 (H-3) _D → (L+2) _D	$\pi\pi^*$
		0.30 (H-2) _D → (L+3) _D	
T ₂	3.19	0.32 (H-3) _D → (L+3) _D	$\pi\pi^*$
		0.30 (H-2) _D → (L+2) _D	
T ₃	3.42	0.38 H _D → L _D	$n\pi^*$
		0.37 (H-1) _D → (L+1) _D	
T ₄	3.42	0.38 H _D → (L+1) _D	$n\pi^*$
		0.37 (H-1) _D → L _D	
Exciton state in <i>ababab</i> dimer (D2)			
State	Exc. Energy/eV	Wavefunction	Nature
T ₁	3.19	0.33 (H-3) _D → (L+3) _D	$\pi\pi^*$
		0.32 (H-2) _D → (L+2) _D	
T ₂	3.19	0.32 (H-3) _D → (L+2) _D	$\pi\pi^*$
		0.32 (H-2) _D → (L+3) _D	
T ₃	3.43	0.37 (H-1) _D → L _D	$n\pi^*$
		-0.35 H _D → (L+1) _D	
T ₄	3.43	0.36 (H-1) _D → (L+1) _D	$n\pi^*$
		-0.36 H _D → L _D	

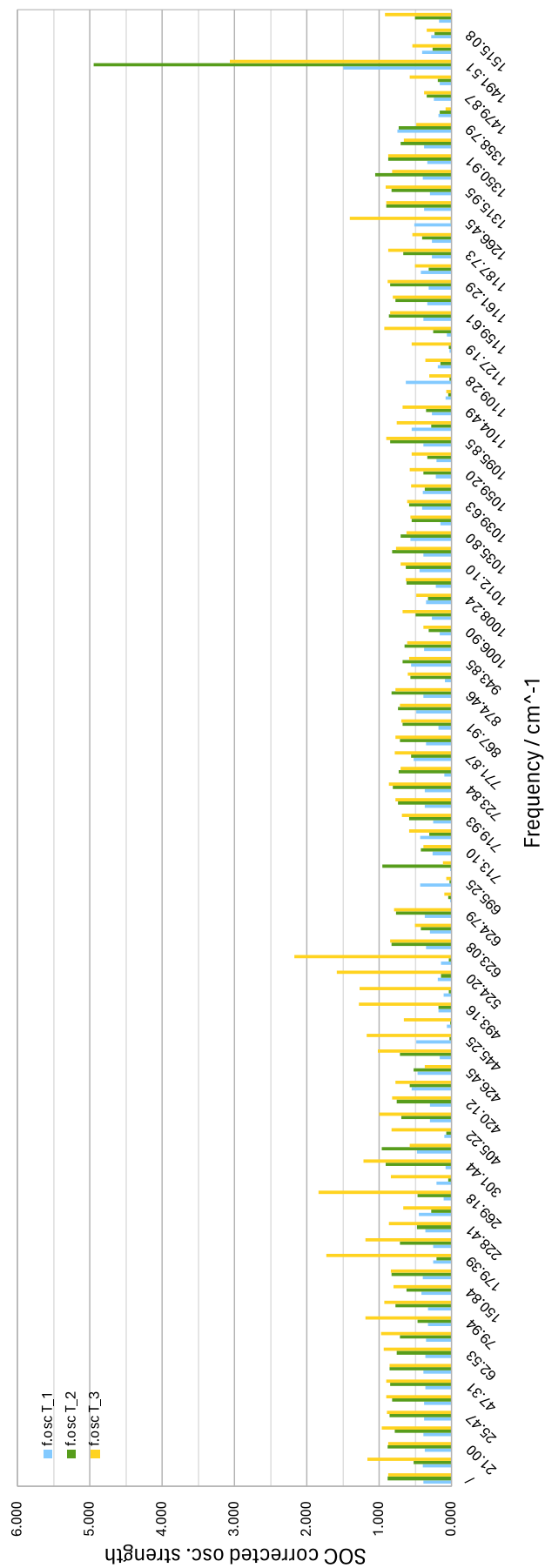
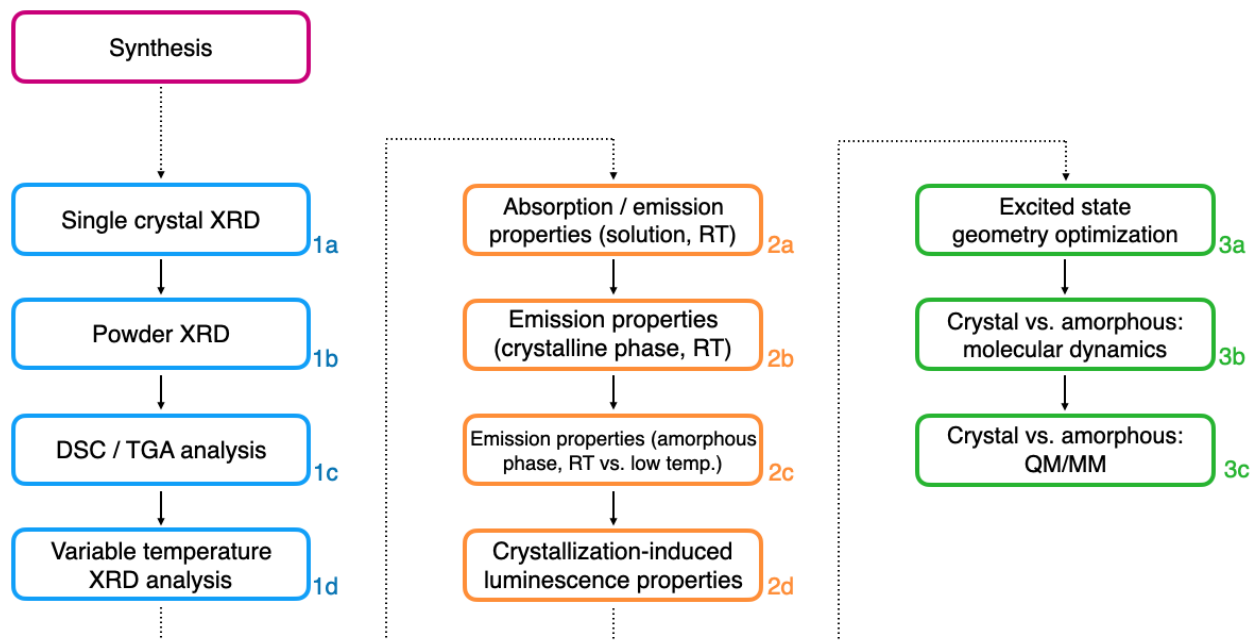


Figure S37. A6-Ph (*ababab* conformer): SOC corrected oscillator strengths of the T₁ π* state by considering the effect of each non-totalsymmetric vibrational mode of the T₁ state (x-axis). The oscillator strengths for the three sublevels of the T₁ state (sky blue: T₁, green: T₂ and yellow: T₃) are considered. TDA-M06-2X/ ZORA-def2-TZVP calculations including 5 singlet and 5 triplet excited states.



Scheme S1. General flow overview for the analysis of structural-related emissive properties of organic solid emitters through structural analysis and thermal characterization (1), photophysical analysis (2) and computational methods (3).

Note: in stage 1a software such as CrysAlis PRO (or equivalents) could be used for data acquisition and elaboration; for structural solution and refinement the OLEX2 software implementing the SHELX method can be employed. For studies on crystal packing, software such as CCDC Mercury are useful to calculate distances and evaluate intra- and intermolecular distances, interactions and calculation of the powder pattern based on the single crystal structure. In stage 1c, software such as XPERT Pro and High Score can be used for data acquisition and elaboration, respectively. Concerning thermal analysis (stages 1c-d), software such as TA Universal Analysis (TA Instruments) can collect and calculate thermal data from TGA and DSC measurements.

For photophysical analysis, we underline the importance of collecting data from crystalline and amorphous phases both at RT and low temperature (stage 2b-c), in order to highlight the relationship between structural factors and the observed luminescence response (stage 2d).

Concerning computational methods, the geometry optimization can be calculated through the GAUSSIAN package, using the TD-M06-2X/def2-SVP level of theory (stage 3a). Molecular dynamics calculations can be achieved with the Tinker software (or equivalents) adopting the NVT ensemble (stage 3b). To highlight differences in the excited state properties between crystalline and amorphous phases (stage 3c), QM/MM calculations were performed with the GAUSSIAN16 package (or equivalents). The QM/MM allow to take into account the influence of surrounding molecules (modeled by molecular mechanics) on the photophysical properties of one central molecule in the solid phase (computed by quantum mechanical approaches).

SUPPORTING REFERENCES

- [1] J. H. R. Tucker, M. Gingras, H. Brand, J.-M. Lehn, *J. Chem. Soc. Perkin Trans. 2* **1997**, 1303–1308.
- [2] G. Bergamini, A. Fermi, C. Botta, U. Giovanella, S. Di Motta, F. Negri, R. Peresutti, M. Gingras, P. Ceroni, *J. Mater. Chem. C* **2013**, *1*, 2717–2724.
- [3] A. Fermi, G. Bergamini, R. Peresutti, E. Marchi, M. Roy, P. Ceroni, M. Gingras, *Dyes Pigm.* **2014**, *110*, 113–122.
- [4] L. Testaferri, M. Tingoli, M. Tiecco, *J. Org. Chem.* **1980**, *45*, 4376–4380.
- [5] G. M. Sheldrick, *Acta Crystallogr. Sect. A Found. Adv.* **2015**, *71*, 3–8.
- [6] G. M. Sheldrick, *Acta Crystallogr. Sect. C Struct. Chem.* **2015**, *71*, 3–8.
- [7] O. V. Dolomanov, L. J. Bourhis, R. J. Gildea, J. A. K. Howard, H. Puschmann, *J. Appl. Crystallogr.* **2009**, *42*, 339–341.
- [8] C. F. Macrae, I. Sovago, S. J. Cottrell, P. T. A. Galek, P. McCabe, E. Pidcock, M. Platings, G. P. Shields, J. S. Stevens, M. Towler, P. A. Wood, *J. Appl. Crystallogr.* **2020**, *53*, 226–235.
- [9] J. C. De Mello, H. F. Wittmann, R. H. Friend, *Adv. Mater.* **1997**, *9*, 230–232.
- [10] S. Grimme, J. Antony, S. Ehrlich, H. Krieg, *J. Chem. Phys.* **2010**, *132*, 154104.
- [11] P. Pracht, F. Bohle, S. Grimme, *Phys. Chem. Chem. Phys.* **2020**, *22*, 7169–7192.
- [12] C. Bannwarth, S. Ehlert, S. Grimme, *J. Chem. Theory Comput.* **2019**, *15*, 1652–1671.
- [13] C. Bannwarth, E. Caldeweyher, S. Ehlert, A. Hansen, P. Pracht, J. Seibert, S. Spicher, S. Grimme, *WIREs Comput. Mol. Sci.* **2021**, *11*, 1–49.
- [14] B. de Souza, G. Farias, F. Neese, R. Izsák, *J. Chem. Theory Comput.* **2019**, *15*, 1896–1904.
- [15] F. Neese, *J. Chem. Phys.* **2005**, *122*, 034107.
- [16] E. van Lenthe, J. G. Snijders, E. J. Baerends, *J. Chem. Phys.* **1996**, *105*, 6505–6516.
- [17] F. Neese, F. Wennmohs, U. Becker, C. Riplinger, *J. Chem. Phys.* **2020**, *152*, 224108.
- [18] M. J. Frisch, G. W. Trucks, H. B. Schlegel, G. E. Scuseria, M. A. Robb, J. R. Cheeseman, G. Scalmani, V. Barone, G. A. Petersson, H. Nakatsuji, X. Li, M. Caricato, A. V. Marenich, J. Bloino, B. G. Janesko, R. Gomperts, B. Mennucci, H. P. Hratchian, J. V. Ortiz, A. F. Izmaylov, J. L. Sonnenberg, D. Williams-Young, F. Ding, F. Lipparini, F. Egidi, J. Goings, B. Peng, A. Petrone, T. Henderson, D. Ranasinghe, V. G. Zakrzewski, J. Gao, N. Rega, G. Zheng, W. Liang, M. Hada, M. Ehara, K. Toyota, R. Fukuda, J. Hasegawa, M. Ishida, T. Nakajima, Y. Honda, O. Kitao, H. Nakai, T. Vreven, K. Throssell, J. A. Montgomery Jr., J. E. Peralta, F. Ogliaro, M. J. Bearpark, J. J. Heyd, E. N. Brothers, K. N. Kudin, V. N. Staroverov, T. A. Keith, R. Kobayashi, J. Normand, K. Raghavachari, A. P. Rendell, J. C. Burant, S. S. Iyengar, J. Tomasi, M. Cossi, J. M. Millam, M. Klene, C. Adamo, R. Cammi, J. W. Ochterski, R. L. Martin, K. Morokuma, O. Farkas, J. B. Foresman, D. J. Fox, *Gaussian, Inc., Wallingford CT*, **2019**.
- [19] J. H. Lii, N. L. Allinger, *J. Am. Chem. Soc.* **1989**, *111*, 8566–8575.
- [20] H. J. C. Berendsen, J. P. M. Postma, W. F. van Gunsteren, A. DiNola, J. R. Haak, *J. Chem. Phys.* **1984**, *81*, 3684–3690.
- [21] L. Martínez, R. Andrade, E. G. Birgin, J. M. Martínez, *J. Comput. Chem.* **2009**, *30*, 2157–2164.
- [22] J. A. Rackers, Z. Wang, C. Lu, M. L. Laury, L. Lagardère, M. J. Schnieders, J.-P. Piquemal, P. Ren, J. W. Ponder, *J. Chem. Theory Comput.* **2018**, *14*, 5273–5289.
- [23] S. Dapprich, I. Komáromi, K. S. Byun, K. Morokuma, M. J. Frisch, *J. Mol. Struct. THEOCHEM* **1999**, *461–462*, 1–21.
- [24] A. K. Rappe, W. A. Goddard, *J. Phys. Chem.* **1991**, *95*, 3358–3363.
- [25] S. L. Mayo, B. D. Olafson, W. A. Goddard, *J. Phys. Chem.* **1990**, *94*, 8897–8909.